

## Nanoparticle Uptake in a Spontaneous and Immunocompetent Woodchuck Liver Cancer Model

Lewis Y. Liu, Xue-Zhong Ma, Ben Ouyang, Danielle P. Ings, Sagar Marwah, Jeff Liu, Annie Y. Chen, Rahul Gupta, Justin Manuel, Xu-Chun Chen, Blair K. Gage, Iulia Cirlan, Nicholas Khuu, Sai Chung, Damra Camat, Michael Cheng, Manmeet Sekhon, Kyril Zagorovsky, Mohamed A. Abdou Mohamed, Cornelia Thoeni, Jawairia Atif, Juan Echeverri, Dagmar Kollmann, Sandra Fischer, Gary D. Bader, Warren C.W. Chan, Tomasz I. Michalak, Ian D. McGilvray, and Sonya A. MacParland

*ACS Nano*, **Just Accepted Manuscript** • DOI: 10.1021/acsnano.0c00468 • Publication Date (Web): 07 Apr 2020

Downloaded from [pubs.acs.org](https://pubs.acs.org) on April 8, 2020

### Just Accepted

“Just Accepted” manuscripts have been peer-reviewed and accepted for publication. They are posted online prior to technical editing, formatting for publication and author proofing. The American Chemical Society provides “Just Accepted” as a service to the research community to expedite the dissemination of scientific material as soon as possible after acceptance. “Just Accepted” manuscripts appear in full in PDF format accompanied by an HTML abstract. “Just Accepted” manuscripts have been fully peer reviewed, but should not be considered the official version of record. They are citable by the Digital Object Identifier (DOI®). “Just Accepted” is an optional service offered to authors. Therefore, the “Just Accepted” Web site may not include all articles that will be published in the journal. After a manuscript is technically edited and formatted, it will be removed from the “Just Accepted” Web site and published as an ASAP article. Note that technical editing may introduce minor changes to the manuscript text and/or graphics which could affect content, and all legal disclaimers and ethical guidelines that apply to the journal pertain. ACS cannot be held responsible for errors or consequences arising from the use of information contained in these “Just Accepted” manuscripts.

# Nanoparticle Uptake in a Spontaneous and Immunocompetent Woodchuck Liver Cancer Model

## AUTHOR NAMES

*Lewis Y. Liu<sup>1,2</sup>, Xue-Zhong Ma<sup>1</sup>, Ben Ouyang<sup>3</sup>, Danielle P. Ings<sup>4</sup>, Sagar Marwah<sup>1</sup>, Jeff Liu<sup>5</sup>, Annie Y. Chen<sup>4</sup>, Rahul Gupta<sup>1</sup>, Justin Manuel<sup>1</sup>, Xu-Chun Chen<sup>1</sup>, Blair K. Gage<sup>1,6</sup>, Iulia Cirlan<sup>7</sup>, Nicholas Khuu<sup>7</sup>, Sai Chung<sup>1,2</sup>, Damra Camat<sup>1,2</sup>, Michael Cheng<sup>1,8</sup>, Manmeet Sekhon<sup>1</sup>, Kyril Zagorovsky<sup>3,8</sup>, Mohamed A. Abdou Mohamed<sup>8,9</sup>, Cornelia Thoeni<sup>1</sup>, Jawairia Atif<sup>1,2</sup>, Juan Echeverri<sup>1</sup>, Dagmar Kollmann<sup>1</sup>, Sandra Fischer<sup>1,10</sup>, Gary D. Bader<sup>5</sup>, Warren C.W. Chan<sup>3,11</sup>, Tomasz I. Michalak<sup>\*4</sup>, Ian D. McGilvray<sup>\*1</sup>, Sonya A. MacParland<sup>\*1,2,10</sup> (\*co-senior to whom correspondence should be addressed)*

## AUTHOR ADDRESS

<sup>1</sup> Soham & Shaila Ajmera Family Transplant Centre, Toronto General Research Institute, University Health Network, 200 Elizabeth Street, Toronto, Ontario, Canada, M5G 2C4

<sup>2</sup> Department of Immunology, University of Toronto, Medical Sciences Building, Room 6271, 1 King's College Circle, Toronto, Ontario, Canada, M5S 1A8

<sup>3</sup> Institute of Biomaterials and Biomedical Engineering, University of Toronto, Rosebrugh Building, Room 407, 164 College Street, Toronto, Ontario, Canada, M5S 3G9

<sup>4</sup> Molecular Virology and Hepatology Research Group, Faculty of Medicine, Health Sciences Centre, Memorial University, 300 Prince Philip Drive, St. John's, Newfoundland, Canada, A1B 3V6

<sup>5</sup> Terrence Donnelly Centre for Cellular and Biomolecular Research, University of Toronto, 160 College Street, Room 230, Toronto, Ontario, Canada, M5S 3E1

<sup>6</sup> McEwen Stem Cell Institute, University Health Network, Toronto, ON, Canada, M5G 1L7

<sup>7</sup> Princess Margaret Genomics Centre, University Health Network, Toronto, Ontario, M5G 1L7

<sup>8</sup> Luna Nanotech, Toronto, Ontario, Canada, M5G 1Y8

<sup>9</sup> Botany and Microbiology Department, Faculty of Science, Zagazig University, Zagazig, Egypt, 44519

<sup>10</sup> Department of Laboratory Medicine and Pathobiology, University of Toronto, Medical Sciences Building, Room 6271, 1 King's College Circle, Toronto, Ontario, Canada, M5S 1A8

<sup>11</sup> Department of Materials Science and Engineering, University of Toronto, 160 College Street, Room 450, Toronto, Ontario, Canada, M5S 3E1

1  
2  
3  
4  
5  
6  
7  
8  
9  
10  
11  
12  
13  
14  
15  
16  
17  
18  
19  
20  
21  
22  
23  
24  
25  
26  
27  
28  
29  
30  
31  
32  
33  
34  
35  
36  
37  
38  
39  
40  
41  
42  
43  
44  
45  
46  
47  
48  
49  
50  
51  
52  
53  
54  
55  
56  
57  
58  
59  
60

## ABSTRACT

There is a tremendous focus on the application of nanomaterials for the treatment of cancer. Non-primate models are conventionally used to assess the biomedical utility of nanomaterials. However, these animals often lack an intact immunological background and the tumors in these animals do not develop spontaneously. We introduce a pre-clinical woodchuck hepatitis virus (WHV) induced liver cancer model as a platform for nanoparticle (NP)-based *in vivo* experiments. Liver cancer development in these out-bred animals occurs as a result of persistent viral infection, mimicking human hepatitis B virus (HBV)-induced HCC development. We highlight how this model addresses key gaps associated with other commonly used tumor models. We employed this model to: (1) Track organ biodistribution of gold NPs after intravenous administration; (2) Examine their subcellular localization in the liver; (3) Determine clearance kinetics, and (4) Characterize the identity of hepatic macrophages that take up NPs using RNA-sequencing (RNA-seq). We found that the liver and spleen were the primary sites of NP accumulation. Subcellular analyses revealed accumulation of NPs in the lysosomes of CD14<sup>+</sup> cells. Through RNA-seq, we uncovered that immunosuppressive macrophages within the woodchuck liver are the major cell type that take up injected NPs. The woodchuck-HCC model has the potential to be an invaluable tool to examine NP-based immune modifiers that promote host anti-tumor immunity.

KEYWORDS: marmota monax, hepatocellular carcinoma, gold nanoparticles, tumor microenvironment, biodistribution, woodchuck hepatitis virus

1  
2  
3  
4 A major barrier to understanding and targeting liver cancer is that there is a paucity of animal  
5  
6 models that faithfully recapitulate the development of human primary hepatocellular carcinoma  
7  
8 (HCC) on an intact immunological background. Given that ~80% of HCC cases result from  
9  
10 chronic hepatitis B or C virus infection,<sup>1</sup> an attractive pre-clinical animal model to test HCC  
11  
12 therapies is the well-established woodchuck hepatitis virus (WHV)-induced HCC.<sup>2,3</sup> In brief, the  
13  
14 eastern North American woodchuck (*Marmota monax*) naturally or experimentally infected with  
15  
16 WHV can establish chronic hepatitis that naturally (spontaneously) progresses to HCC.<sup>4</sup> The  
17  
18 viral life cycles of WHV and HBV are very similar and both viruses share up to 70% nucleotide  
19  
20 homology.<sup>5,6</sup> We compared the genomes of woodchucks and humans using BLASTp<sup>7</sup> and found  
21  
22 that 90% of woodchuck protein sequences show significant similarity to proteins in the human  
23  
24 genome, indicating a high degree of sequence homology at the protein level (Supplementary  
25  
26 Table 1). As such, the woodchuck model has been used to validate the effectiveness of nearly  
27  
28 every single FDA approved antiviral for the treatment of chronic HBV infection in humans, such  
29  
30 as lamivudine, entecavir, tenofovir disoproxil fumarate, telbivudine, and adefovir dipivoxil.<sup>8-14</sup>  
31  
32  
33  
34  
35  
36 The overall high success rate of approved therapeutics indicates that the woodchuck animal  
37  
38 model can be employed as a robust predictor of therapy success in clinic. Currently, this is the  
39  
40 only *in vivo* experimental system that incorporates and effectively models the viral infection, the  
41  
42 subsequent development of HCC, and the immune response against both virus and tumor.

43  
44  
45 Although infected woodchucks do not develop cirrhosis and ascites, which frequently  
46  
47 accompany HCC in HBV-infected humans, they recapitulate the prevailing mechanisms of  
48  
49 human hepatocarcinogenesis related to virus integration, and chronic necroinflammation  
50  
51 damaging hepatocytes and their cycles of regeneration. Mouse models of liver carcinogenesis do  
52  
53 not fully incorporate tumor development in the context of chronic hepatitis on an intact  
54  
55  
56  
57  
58  
59  
60

1  
2  
3 immunological background (Figure 1A).<sup>15-17</sup> For example, tumors that develop from chemically  
4  
5 treated animals lack key drivers of human hepatitis-induced hepatocarcinogenesis that are  
6  
7 characteristic of WHV and HBV chronic infections.<sup>16, 18</sup> Several non-mouse models of HCC,  
8  
9 such as those from rabbit, pig, or rat, also fail to recapitulate human virally-induced HCC.<sup>19-25</sup>  
10  
11 Specific caveats of these models and how the woodchuck HCC model addresses these  
12  
13 deficiencies have been summarized in Figure S1A and S1B.  
14  
15  
16  
17

18  
19 At the molecular level, several subtypes of HCC in humans resulting from chronic HBV  
20  
21 infection have been recognized, such as the common S2<sup>26</sup> and “poor survival” subtypes<sup>27</sup> or the  
22  
23 less common S3 and G5 subtypes. The molecular profile of WHV-induced HCC was found most  
24  
25 closely reflecting the common subtypes, but not the S3 and G5 subtypes.<sup>28</sup> This indicates that at  
26  
27 the molecular level, woodchuck HCC is fundamentally similar to the more common subtypes of  
28  
29 HCC in humans. While other tumor models may provide a basis to study select components of  
30  
31 the underlying intracellular signaling pathways, the majority are unable to uncover the more  
32  
33 detailed picture of the signaling alterations that occur during the step-wise progression of viral  
34  
35 hepatitis-induced HCC. Given that one of the major issues that impedes the successful clinical  
36  
37 translation of pre-clinical animal models is the lack of tumor models that accurately recapitulate  
38  
39 human cancers,<sup>29, 30</sup> the woodchuck model of HCC provides a pathobiologically relevant *in vivo*  
40  
41 system that can be used to investigate therapeutic platforms for HCC and other liver disease.  
42  
43  
44  
45  
46  
47

48  
49 The importance of using an animal model that closely resembles the disease course in humans is  
50  
51 highlighted when investigating how cancer therapies will likely behave within the human tumor  
52  
53 microenvironment (TME). The TME is a tumor-supportive niche that has been shown to exist in  
54  
55 various solid cancers such as those of breast, lung, and colon.<sup>31-35</sup> In particular, tumor-associated  
56  
57

1  
2  
3 macrophages (TAMs) are a major cellular component of the TME which play a pivotal role in  
4  
5 determining tumor fate.<sup>32</sup> The balance between inflammatory (tumoricidal) and  
6  
7 immunoregulatory (tumor promoting) TAMs controls tumor development, progression, and  
8  
9 metastasis.<sup>36-38</sup> Furthermore, different ratios of tumoricidal to tumor promoting TAMs have been  
10  
11 identified to be important prognostic factor in cancer patients.<sup>39-41</sup> The identification of therapies  
12  
13 that can target tumor promoting TAMs may serve as a valuable approach to prevent the  
14  
15 development and/or progression of solid tumors by promoting anti-tumor immunity within the  
16  
17 TME.  
18  
19  
20  
21  
22

23 One approach is to use nanoparticles (NPs). NPs are a promising therapeutic strategy for tumor-  
24  
25 cell homing and drug-payload delivery. The idea of targeting one's own immune cells has been  
26  
27 validated as a promising therapeutic approach as well.<sup>42, 43</sup> In particular, macrophage plasticity  
28  
29 has recently been shown to be exploitable with NPs<sup>44-46</sup> and understanding the key regulatory  
30  
31 networks that govern macrophage uptake as well as phenotype and function will be essential for  
32  
33 improving NP design. Furthermore, since our intended target is actually not the cancer cells  
34  
35 themselves but macrophages, which are known to also sequester NPs, this therapeutic approach  
36  
37 may circumvent issues associated with cancer cell drug resistance and clearance of anti-  
38  
39 cancerous drugs.<sup>47, 48</sup>  
40  
41  
42  
43

44 The woodchuck model allows for the ability to home in on NP-TME interactions that are likely  
45  
46 more representative of HBV-induced hepatocarcinogenesis in humans. Indeed, the complex  
47  
48 dynamics of the tumor vasculature and microenvironment has been shown to impact NP  
49  
50 accumulation, penetration and ultimately therapeutic efficacy.<sup>49-53</sup> In the context of HCC, the  
51  
52 pre-clinical woodchuck model of virally induced HCC provides an ideal system to study the  
53  
54 efficacy of NP-based HCC therapeutics because WHV-induced HCC shares a highly similar  
55  
56  
57

1  
2  
3 disease course as HBV-induced HCC and preserves the local TME, and the host's natural  
4 immunobiological background.  
5  
6  
7  
8

## 9 RESULTS AND DISCUSSION:

10  
11 To establish the basis for the use of NPs in this pre-clinical animal system, we injected 14 mg/kg  
12 of 60-nm gold NPs *via* intravenous injection into 7 woodchucks (3 healthy, 4 WHV-positive  
13 tumor bearing) to assess the biodistribution, cellular uptake, and subcellular localization of these  
14 particles. We found that the liver was the primary organ that takes up these particles. NP  
15 subcellular localization was mainly restricted to the lysosomal compartment of CD14<sup>+</sup> cells. This  
16 indicated that the liver is the organ of choice to process and metabolize NPs in the body, and  
17 lysosomes of CD14<sup>+</sup> cells were the main subcellular compartment that sequesters 60-nm gold  
18 NPs. These findings correspond to what has been previously shown in other rodent models and  
19 humans which validates woodchucks as a model for testing of NP therapies.<sup>54-58</sup>  
20  
21  
22  
23  
24  
25  
26  
27  
28  
29  
30  
31

### 32 Experimental Outline and Summary of Experimental Techniques.

33  
34 The experimental outline and time points for the *in vivo* injection experiments are shown in  
35 Figure 1B. Blood was collected at four time points including a pre-injection control (T=0). In  
36 order to identify the biodistribution of injected NPs first at the organ level, we harvested whole  
37 organs for analysis using inductive coupled mass spectrometry (ICP-MS). Next, to identify the  
38 cellular localization of injected NPs, we performed flow cytometry on tissue homogenates from  
39 dissociated liver and lung tissues of healthy and WHV-infected animals. We used both electron  
40 and confocal microscopy to identify the subcellular localization of these particles at 12 h post-  
41 injection (p.i). Finally, we performed RNA-seq on cells dissociated from liver tissue, with a  
42 focus on CD14<sup>+</sup> cells, to investigate the transcriptional differences between the cells that take up  
43 NPs compared to those that do not.  
44  
45  
46  
47  
48  
49  
50  
51  
52  
53  
54  
55  
56  
57  
58  
59  
60

### Characterization of 60-nm Gold Nanoparticles.

Penetration and accumulation in tumor tissue are important factors when considering NP design.<sup>59</sup> 60-nm particles are well-studied in mouse models and allows the comparison of results obtained from our woodchuck animal model to previously studied mouse models.<sup>60-62</sup> In general, gold NPs are also relatively easy to synthesize and can be conjugated with a wide array of surface moieties including fluorophores for downstream analysis. The near infrared dye IR750 was conjugated to the injected NPs making them visible by confocal microscopy and flow cytometry (Figure 2A). Two polyethylene glycol (PEG) sizes were used; 5-kDA and 10-kDA. The IR750 dye was conjugated to the 5-kDA PEG on a backfill of 10-kDA PEG which increased the half-life and stability of the fluorescent molecule in solution. Attaching the IR750 dye to the shorter PEG also minimizes the possible interactions it may have with the biological environment. For example, particle charge has been shown to impact the kinetics and internalization of NPs by phagocytic cells like macrophages,<sup>63, 64</sup> therefore shielding the dye from the biological environment minimizes potential charge-mediated effects. Additional information on characterization parameters is summarized in Figure 2B and Figure S2. The injected NPs are notably stable and remain intact after injection as shown by electron microscopy of woodchuck liver tissue (Figure 2C). Once the biodistribution of gold NPs has been established in woodchucks, we will eventually test biocompatible particles that will be geared towards therapeutic translation.

### Biodistribution of Intravenously Injected NPs in Healthy and WHV-Infected Woodchucks.

We investigated the biodistribution of intravenously injected NPs in woodchucks at the cellular and organ level using flow cytometry (Figure 3A, 3Biv-v, and 3Civ-v) and ICP-MS (Figures

1  
2  
3 3Bi-iii and 3Ci-iii). Organ tissue was isolated from healthy and WHV-positive woodchucks. In  
4 the healthy animal group (n=3), we found that the liver is the primary organ that takes up 60-nm  
5 gold NPs when compared to other organs (Figure 3Bi). As expected, the spleen also accumulated  
6 a significant amount of gold NPs but only made up a fraction of the total injected dose because  
7 the spleen was much smaller than the liver (Figure 3Bii). These results were very similar to  
8 previous biodistribution experiments in rodents.<sup>54, 65</sup> A negligible quantity of NPs were detected  
9 in the urine 12 h p.i. indicating that the injected particles were not excreted *via* kidneys (Figure  
10 3Biii). This was consistent with previous NP elimination studies in mice that showed that  
11 particles greater than 5.5-nm in diameter cannot be excreted through the kidneys.<sup>66, 67</sup> In addition,  
12 given the significant decrease of circulating NPs in blood between 5 min and 12 h p.i with  
13 negligible uptake in any organ except for the liver and spleen, we suspect that the majority of the  
14 circulating NPs were sequestered by these two organs (Figure 3Biii).

15  
16  
17  
18  
19  
20  
21  
22  
23  
24  
25  
26  
27  
28  
29  
30 We performed flow cytometry to investigate the distribution of injected NPs in different immune  
31 cell types. Woodchuck cross-reactive anti-CD14 and anti-CD3 antibodies (Figure S3) were used  
32 to compare the uptake of NPs in macrophages and T cells, respectively. We investigated  
33 macrophages because they are known to sequester large amounts of NPs in mice and humans.  
34 We investigated T cells because they are known to mediate hepatocyte destruction in HBV. Also,  
35 previous studies have shown that T cells do not take up injected NPs and we wanted to confirm  
36 this in woodchuck.<sup>68</sup> We observed that <5% of T cells took up NPs, while up to 63.4% of CD14<sup>+</sup>  
37 cells took up NPs (Figure 3A). This trend was also observed in the lung and blood (Figure 3Biv).  
38 Relative mean fluorescence intensity (MFI), a proxy for NP abundance, and the percentage of  
39 CD14<sup>+</sup> cells that took up NPs from all healthy animals are summarized (Figure 3Bv). The liver  
40 had the highest relative MFI and percentage of NP-positive CD14<sup>+</sup> cells when compared to lung  
41 and blood. These trends were also observed in WHV-infected animals (n=4) (Figure 3Ci-v). For  
42  
43  
44  
45  
46  
47  
48  
49  
50  
51  
52  
53  
54  
55  
56  
57  
58  
59  
60

1  
2  
3 instance, of the CD14<sup>+</sup> cells isolated from the liver, lung and PBMC of chronically infected  
4  
5 animals, 51.0%, 22.6%, and 1.05%, respectively, had taken up NPs. These results suggest that  
6  
7 the total injected dose of gold NPs was primarily concentrated in the liver and that CD14<sup>+</sup> cells  
8  
9 were able to take up injected NPs up to approximately 30 times more than T cells isolated from  
10  
11 the woodchuck liver in both animal groups. Additional gating strategies for all experiments are  
12  
13 provided in Figure S3 and general gating strategy is provided in Figure 3A.  
14  
15

16  
17 In order to assess NP biodistribution and the kinetics of particle sequestration by the organs over  
18  
19 a longer time period, preliminary experiments using three additional animals (1 healthy, 2 WHV-  
20  
21 infected) treated with 60-nm gold NPs for 48 h p.i. were conducted (Figure S4). Our results  
22  
23 indicate that there was approximately 40% more uptake (50-70% injected dose) of NPs by the  
24  
25 liver at 48 h p.i. compared to 12 h p.i. in both animal groups (Figures S4Ai, S4Bi, and S4C). This  
26  
27 suggests that circulating NPs continue to become sequestered by the liver up to 48 h p.i. These  
28  
29 results are consistent with previous biodistribution experiments in mice where approximately  
30  
31 70% of the injected dose was found in the liver after 1 day post-infusion with gold-based  
32  
33 nanorods.<sup>69</sup> The average particle half-life was approximately 7.5 h and 3.7 h for WHV-infected  
34  
35 and healthy animals, respectively (Figures S4Aii and S4Bii). We measured the amount of gold in  
36  
37 bile and feces at 48 h p.i. by ICP-MS (Figures S4Ai and S4Bi). A negligible amount (<0.0001%  
38  
39 injected dose) of gold was detected, indicating that at 48 h p.i, 60-nm gold NPs remain  
40  
41 sequestered in the liver and were not readily excreted through the hepatobiliary route. These  
42  
43 findings are consistent with other studies in mice. For example, the elimination of 50-nm  
44  
45 PEGylated gold NPs in mice through the hepatobiliary pathway was low, between 0.2-1.0% of  
46  
47 total injected dose.<sup>67</sup>  
48  
49  
50  
51  
52  
53  
54  
55

56 Histopathological Evaluation of Woodchuck HCC.  
57

1  
2  
3 The NP biodistribution patterns described above in WHV-induced chronic hepatitis can only be  
4 applied to human disease if WHV and HBV cause similar patterns of liver damage at a  
5 histological level. Chronic HBV infection causes necrosis in the periportal and, when severe,  
6 intralobular hepatocytes which disrupts the liver architecture. In the WHV-infected woodchuck  
7 livers, we observed a similar histological pattern (Figure S5A), confirming that inflammation-  
8 mediated hepatocyte damage occurs both in woodchucks and humans, as described.<sup>2,3</sup> Indeed, it  
9 is well established that T lymphocyte-mediated hepatocyte destruction contribute to the overall  
10 picture of chronic hepatitis in woodchucks and humans.<sup>70</sup> Our results also indicate that T cells  
11 are recruited to sites of inflammation including the junction between tumor and non-tumor tissue  
12 (Figure S5Bi-vi). This was not caused by the injected NPs since the healthy animals did not  
13 develop such lesions following administration of NPs. The histological features were common  
14 between woodchucks used in this study and tumor histomorphology was consistent between  
15 tumors from different animals and between tumors from the same animal (multi-focal HCC).  
16 This suggests that the HCCs that develop in woodchuck including the observed T cell  
17 distribution patterns are fairly homogenous. Finally, we also investigated the differences between  
18 healthy and HCC liver architecture using scanning electron microscopy (Figure S6). We noted  
19 that, just like human HCC, distinct liver fenestrations were lost in HCC (Figure S6B) compared  
20 to healthy liver (Figure S6A). These results further indicated that WHV-induced HCC is highly  
21 similar to HBV-induced HCC, as reported,<sup>5</sup> and validates the woodchuck model as an excellent  
22 biological system to test NP-based therapies.

#### 51 Identifying the Subcellular Localization of Injected NPs.

52  
53 Having established the biodistribution of 60-nm gold NPs at the organ and cellular level in  
54 healthy and WHV-infected woodchucks, we next investigated the subcellular localization of the  
55  
56  
57

1  
2  
3 injected NPs. Thus, transmission electron microscopy (TEM) was applied to visualize the  
4  
5 subcellular structures of bulk tissue segments and confocal microscopy was used on magnetically  
6  
7 sorted CD14<sup>+</sup> cells isolated from the woodchuck liver (Figure 4). We observed no uptake of NPs  
8  
9 by hepatocytes using TEM after analyzing the tissue sections taken from the HCC uninvolved  
10  
11 liver, tumor adjacent tissue, and tumor of three chronic animals and the liver of 3 healthy  
12  
13 animals. We observed that macrophages lining the sinusoid of healthy and infected but HCC  
14  
15 uninvolved liver tissue took up NPs (Figure 4Ai-ii and 4Bi-ii). These NPs appeared to  
16  
17 accumulate in lysosomal compartments. We observed this in TAMs as well (Figure 5Biii). We  
18  
19 confirmed this finding using confocal microscopy in healthy (Figure 4C) and WHV-infected  
20  
21 animals (Supplemental Video 1). These findings indicated that hepatic CD14<sup>+</sup> cells preferentially  
22  
23 take up injected gold NPs and that these particles are located in cytoplasmic lysosomal vesicles.  
24  
25  
26  
27  
28 Given that the subcellular distribution pattern of our injected particles showed confinement to  
29  
30 lysosomes, the utilization of pH-sensitive therapeutic particles would be a potential future area of  
31  
32 interest in the design of NPs that modulate macrophage function. Indeed, several of these  
33  
34 formulations have already been studied and validated in both *in vitro* and *in vivo* settings.<sup>71-73</sup>  
35  
36  
37  
38

### 39 Distribution of Injected NPs in Different Areas of the Tumor and Tumor Interface.

40  
41 Having characterized the biodistribution of the injected NPs at the organ, cellular and subcellular  
42  
43 levels, we next investigated the dispersion of particles throughout the tumor and at the interface  
44  
45 between non-tumorous and tumor tissue. The tumor core was taken by removing a segment of  
46  
47 tissue (about one cm<sup>3</sup>) from the center of the tumor, while the tumor periphery included a piece  
48  
49 of tissue near the tumor capsule at the invading edge. ICP-MS was performed on these two tissue  
50  
51 compartments (core and periphery) for all tumors. The accumulation of gold at the tumor  
52  
53 periphery was significantly greater than that of the core (Figure 5Ai). This data corresponded  
54  
55  
56  
57

1  
2  
3 well with results from other studies investigating particle or dye distribution as a function of  
4 tumor vasculature.<sup>52, 60, 74</sup> Indeed, other formulations, such as liposomes and antibody-based  
5 therapies, are also known to show similar peripheral distribution patterns in mice.<sup>53, 75</sup> To provide  
6 a more detailed assessment of gold NP distribution within the tumor and the non-tumor-tumor  
7 interface, multiple tissue segments (about one cm<sup>3</sup> each), ranging from the tumor core to the  
8 surrounding normal liver tissue, were isolated for ICP-MS analysis as shown in Figure 5Aii. In  
9 this figure, increasing numerical value represents increasing distance from the tumor core while  
10 each of the 9 tissue segments roughly estimates the distance from the tumor core in centimeters.  
11 For example, segments 3 is about 3 cm from the tumor core but still contained within the tumor  
12 capsule, while segment 8 is non-tumorous liver tissue that is about 8 cm away from the tumor  
13 core. A picture of the tissue segments used for analysis is provided in Figure S7Ai-ii. We  
14 observed a significant ( $p=0.0149$ ) increase in gold NP uptake at the tumor periphery (segments  
15 5) compared to the inner area of the tumor such as segment 4. Given that macrophages within the  
16 tumor did show discrete accumulation of NPs in lysosomes (Figure 5Aiii) and that a large  
17 majority of TAMs took up NPs (Figure 5Bi-iii and Figure S8), we hypothesized that the apparent  
18 decrease in gold abundance in the tumor seen in Figure 5Ai-ii could be a result of the abundance  
19 of macrophages penetrating the tumor. To answer this question, we performed  
20 immunohistochemistry (IHC) staining using CD68 as a marker for liver resident macrophages  
21 (Figure 5C). Although both CD14 and CD68 IHC staining were performed, only staining with  
22 the polyclonal CD68 antibody produced expected patterns of specific staining as assessed by a  
23 liver pathologist. Using CD14 to stain for monocytes/macrophages resulted in high levels of  
24 background staining which did not allow for the identification of monocyte/macrophage  
25 population in the woodchuck liver. Interestingly, we found that there was more CD68<sup>+</sup> cells in  
26 the uninvolved liver of HCC-bearing woodchucks compared to the tumor. This suggests that the

1  
2  
3 decrease in NP accumulation observed in the tumor may, at least in part, be mediated by a higher  
4 amount of CD68<sup>+</sup> cells in uninvolved tissue. Our finding with respect to the low uptake and poor  
5 penetration of NPs in HCC tumors provides a possible explanation on why previous attempts  
6 using HCC therapeutics such as NP-based doxorubicin in HCC patients were relatively  
7 unsuccessful.<sup>76</sup> Since macrophages are the primary cell type that take up intravenously injected  
8 NPs, targeting TAMs surrounding the tumor by re-polarizing these TAMs into a more  
9 inflammatory phenotype to promote anti-tumor immunity may be a viable approach to treat liver  
10 cancer. Indeed, NP-mediated repolarization of macrophages has already been shown to be  
11 feasible in numerous studies.<sup>46, 77-79</sup> Furthermore, NPs with hydrodynamic (HD) size of ~100nm  
12 have been shown to accumulate in macrophages effectively.<sup>80</sup> Our NP with core size 60nm and  
13 HD of 103.6nm are consistent with these findings as they are avidly taken up by macrophages in  
14 the woodchuck liver. Although our primary target is macrophages, future studies will  
15 characterize the effect(s) of NP size on woodchuck macrophages and HCC tumor targeting to  
16 determine the optimal size of therapeutic NPs. Our results demonstrate that the naturally  
17 augmented uptake of 60-nm gold NPs by the liver in the spontaneously occurring WHV-induced  
18 HCC model may have value for the development and testing of immunomodulatory interventions  
19 based on intravenous delivery of NPs for treating and preventing HCC.  
20  
21  
22  
23  
24  
25  
26  
27  
28  
29  
30  
31  
32  
33  
34  
35  
36  
37  
38  
39  
40  
41  
42  
43

#### 44 Transcriptome Analysis of FACS Sorted NP<sup>+/-</sup> Cells.

45  
46 We next investigated how macrophage phenotype may impact NP uptake. We performed  
47 fluorescence activated cell sorting (FACS) analysis on dissociated, live cells from the uninvolved  
48 liver of a WHV-positive tumor bearing animal and sorted into 4 groups: CD14<sup>+</sup>NP<sup>-</sup>, CD14<sup>-</sup>NP<sup>-</sup>,  
49 CD14<sup>-</sup>NP<sup>+</sup>, and CD14<sup>+</sup>NP<sup>+</sup> (Figure S9Ai-iii). We profiled the molecular signatures of these four  
50 cell populations using RNA-seq (Figure 6A). To focus primarily on the CD14<sup>+</sup> compartment, we  
51  
52  
53  
54  
55  
56  
57  
58  
59  
60

1  
2  
3 first gated out lymphocytes that were CD3<sup>+</sup>NP<sup>-</sup> and, as expected, the large majority of CD3<sup>+</sup> cells  
4  
5 were indeed NP<sup>-</sup>. We also observed an enrichment of *CD14* gene expression in the CD14<sup>+</sup>NP<sup>-</sup>  
6  
7 and CD14<sup>+</sup>NP<sup>+</sup> cell populations which suggests that the mouse anti-human CD14 antibody  
8  
9 (clone: TUK4) used for cell sorting and flow cytometry analyses was cross-reactive with  
10  
11 woodchuck CD14<sup>+</sup> cells (Figure S9B). To determine if NP uptake by CD14<sup>+</sup> cells is  
12  
13 preferentially associated with a particular molecular signature, we compared the genes that were  
14  
15 differentially expressed between the CD14<sup>+</sup>NP<sup>-</sup> and CD14<sup>+</sup>NP<sup>+</sup> cell populations. Our current  
16  
17 results showed that the CD14<sup>+</sup>NP<sup>-</sup> population was enriched for inflammatory genes, such as  
18  
19 *IL1b*, *SI00A8/9*, and *CXCL8*. The CD14<sup>+</sup>NP<sup>+</sup> population was enriched for immunoregulatory  
20  
21 gene expression, such as *MARCO*, *VSIG4*, *GPNMB*, and *MRC1* (CD206) (Figure 6Ai). This  
22  
23 aligns with our previous work that showed higher NP uptake in immunomodulatory  
24  
25 macrophages, compared to their inflammatory counterparts.<sup>68</sup> The overexpression of *GPNMB*  
26  
27 which encodes a transmembrane glycoprotein has been well established in human breast  
28  
29 cancer.<sup>81</sup> This protein is known to be a potent inhibitor of T cell activation.<sup>82, 83</sup> Given that the  
30  
31 CD14<sup>+</sup>NP<sup>+</sup> cell population was enriched for immunoregulatory markers, including *GPNMB*, this  
32  
33 suggests that this population may also contribute to HCC progression by potentially inhibiting T  
34  
35 cell activation in part by *GPNMB*-mediated mechanisms. Therefore, subsequent experiments  
36  
37 aimed at validating TAM-mediated mechanisms of T cell inhibition will be important to  
38  
39 elucidate their potential role(s) in modulating host anti-tumor immunity. Lastly, the  
40  
41 immunoregulatory nature of the CD14<sup>+</sup> NP<sup>+</sup> population provides further support for the  
42  
43 possibility of using NPs to target immunoregulatory TAMs, which are known to support tumor  
44  
45 growth in the context of HCC.  
46  
47  
48  
49  
50  
51  
52  
53  
54  
55  
56  
57  
58  
59  
60

1  
2  
3 To identify what other cell populations take up injected NPs, we hypothesized that the CD14<sup>-</sup>  
4 NP<sup>+</sup> population could consist of CD14<sup>-</sup>CD68<sup>+</sup> macrophages as it has been shown that hepatic  
5 macrophage expression of CD14 and CD68 are diverse.<sup>84</sup> Given that CD68 is predominantly a  
6 marker of resident macrophages, this population could represent a subset of Kupffer cells within  
7 the woodchuck liver. Although there is no woodchuck cross-reactive CD68 antibody available  
8 for cell sorting or flow-based assays, our RNA-seq results indicated that *CD68* expression is  
9 comparatively enriched in the CD14<sup>-</sup>NP<sup>+</sup> population compared to all other populations (Figure  
10 6Ai). This suggests the CD14<sup>-</sup>NP<sup>+</sup> population is indeed composed primarily of liver resident  
11 macrophages which exhibit a similar tolerogenic transcriptional profile to the CD14<sup>+</sup>NP<sup>+</sup> cell  
12 population. Furthermore, in line with our findings suggesting that the CD14<sup>+</sup>NP<sup>-</sup> population was  
13 an inflammatory monocyte/macrophage population, it is likely that this group of cells also  
14 represents a population of recruited monocytes from peripheral blood, given the comparatively  
15 lower expression of macrophage resident marker CD68 and MRC1 (Figure 6Ai). Another  
16 indicator that suggests this population was recruited from blood is their high expression of  
17 *S100A8* and *S100A9* genes which encode a heterodimer known as calprotectin. Calprotectin has a  
18 well-established role as an inflammatory mediator that is expressed on circulating and recently  
19 recruited monocytes.<sup>85-87</sup>

20  
21  
22  
23  
24  
25  
26  
27  
28  
29  
30  
31  
32  
33  
34  
35  
36  
37  
38  
39  
40  
41  
42  
43  
44 To validate the relative proportions of different immune populations present in our tissue  
45 samples, we employed cell-type identification by estimating relative subsets of RNA transcripts  
46 (CIBERSORT).<sup>88</sup> CIBERSORT deconvolutes RNA-seq data by correlating the relative  
47 abundance of detected transcripts in a sample to a signature gene matrix. We used the previously  
48 developed signature gene matrix LM22,<sup>88</sup> which contains 547 genes that help define 22 different  
49 human hematopoietic cell lineages. Our analysis indicates that both the CD14<sup>-</sup>NP<sup>+</sup> and CD14<sup>+</sup>  
50  
51  
52  
53  
54  
55  
56  
57

1  
2  
3 NP<sup>+</sup> cell populations were enriched for immunoregulatory macrophages (denoted as “M $\phi$  anti-  
4 inflam”), while the CD14<sup>+</sup> NP<sup>-</sup> population was enriched in both monocytes and M0 macrophages  
5 (Figure 6Aii). These findings further support the notion that the degree of NP uptake is  
6 dependent on macrophage phenotype. Although previous studies in other animal models have  
7 suggested that B cells also play a large role in mediating NP uptake,<sup>89, 90</sup> using CIBERSORT to  
8 evaluate the relative cell identity of NP-positive and negative fractions in the more  
9 pathophysiologically relevant woodchuck model of HCC, we found that B and plasma cell  
10 signatures made up one-third of the CD14<sup>-</sup> NP<sup>-</sup> signature. Whereas the proportion of B and  
11 plasma cells in the two NP<sup>+</sup> populations was much lower (up to 8% of total signature). In support  
12 of this, the expression of classical B cell markers (*i.e.*, MS4A1, CD19) from our RNA-seq  
13 analysis were predominately expressed in the CD14<sup>-</sup> NP<sup>-</sup> population (Figure 6Ai). For each  
14 macrophage and B cell subtype listed in Figure 6Aii, the top 10 genes that define an immune cell  
15 sub-set from LM22 and their corresponding expression levels in each of the four FACS sorted  
16 populations were presented as a heatmap (Figure 6Aiii). These findings highlight the selective  
17 nature of our injected NPs since they seem to be largely accumulating in immunoregulatory  
18 macrophages compared to other phagocytic cells, such as inflammatory macrophages or B cells.  
19 This is an important point to consider since only a few studies thus far in mouse tumor models  
20 have shown the ability for NPs to specifically target immunoregulatory macrophages.<sup>91</sup>  
21 Therefore, the woodchuck HCC model may serve as a superior experimental system compared to  
22 mouse and other rodent tumor models for evaluating the efficacy of macrophage-specific gold  
23 NP-based therapeutics as a potential treatment of human HCC.

24  
25  
26  
27  
28  
29  
30  
31  
32  
33  
34  
35  
36  
37  
38  
39  
40  
41  
42  
43  
44  
45  
46  
47  
48  
49  
50  
51 In order to identify the specific differences in biological pathways that may exist between the  
52 sorted cell populations investigated in this study, we performed gene set variation analysis  
53 (GSVA) (Figure 6B). GSVA provides a more robust assessment of pathway variation between  
54  
55  
56  
57

1  
2  
3 heterogenous cell populations and can help highlight important biological differences between  
4  
5 the macrophages that take up NPs compared to those that do not. These results support our  
6  
7 previous findings from this study that the cell populations that took up NPs (CD14<sup>-</sup> NP<sup>+</sup> and  
8  
9 CD14<sup>+</sup> NP<sup>+</sup>) expressed immunosuppressive pathways, such as those involving IL-10, IL-27/6  
10  
11 signaling. Several studies have shown that IL-27-mediated signaling has potent  
12  
13 immunoregulatory function such as inducing PD-L1 expression on naïve T cells<sup>92</sup> and inhibiting  
14  
15 IL-2 production by CD4<sup>+</sup> T cells.<sup>93</sup> In contrast, the CD14<sup>+</sup> NP<sup>-</sup> cell population expressed pro-  
16  
17 inflammatory pathways, such as reactive oxygen generation, tumor necrosis factor super family 1  
18  
19 (TNFSF1) signaling, and symbiont cell killing. Interestingly, previous work identified that  
20  
21 SEMA3A is significantly correlated with HCC recurrence in patients and the metastatic potential  
22  
23 of HCC cancer cell lines.<sup>94</sup> It has been shown that SEMA3A was responsible for enhancing HCC  
24  
25 cell proliferation and acted as a chemoattractant for TAMs into the TME. Our results suggest that  
26  
27 both CD14<sup>-</sup> NP<sup>+</sup> and CD14<sup>+</sup> NP<sup>+</sup> cell populations are enriched in the SEMA3A pathway which  
28  
29 well agrees with our expectation that these populations exhibit characteristics of  
30  
31 immunoregulatory TAMs that are known to promote tumor progression and metastasis.  
32  
33  
34  
35  
36  
37

## 38 CONCLUSION:

39  
40  
41 We demonstrated that intravenously injected 60-nm gold NPs in the woodchuck hepatitis-  
42  
43 induced HCC model 1) primarily accumulate in the liver and spleen 2) are taken up by liver  
44  
45 resident macrophages and are sequestered in lysosomes 3) are not eliminated through the  
46  
47 hepatobiliary route or kidneys at 48 h p.i. and 4) are preferentially taken up by  
48  
49 immunoregulatory macrophages. With respect to NP distribution in woodchuck HCC, NP  
50  
51 abundance decreases from periphery to tumor core. This finding might be attributed to the lower  
52  
53 abundance of macrophages penetrating into the tumor and the ability of macrophages to  
54  
55  
56  
57

1  
2  
3 sequester injected NPs. We also identified that our NPs are concentrated at the tumor margin  
4  
5 which will be a key point in future HCC therapy design. A summary of these findings is  
6  
7 illustrated in Figure 7.  
8

9  
10 The preclinical woodchuck model of primary liver cancer can closely recapitulate the  
11  
12 spontaneous development as well as the disease course of hepatitis-induced HCC. Therefore, this  
13  
14 animal model should be considered as a robust tool for studying the molecular mechanisms that  
15  
16 drive hepatocarcinogenesis and should be used to validate the efficacy of therapeutics in the  
17  
18 treatment of human liver cancer. Future therapeutic strategies aimed at re-polarizing  
19  
20 immunoregulatory macrophages in the local TME may be a viable strategy to promote anti-  
21  
22 tumor immunity and increase accumulation of NPs in the tumor.  
23  
24  
25

## 26 27 METHODS:

### 28 29 Animals and Tissue

30  
31 *In vivo* nanoparticle delivery experiments were performed at the Woodchuck Viral Hepatitis  
32  
33 Research Facility at Memorial University, St. John's, NL, Canada under the approval of the  
34  
35 Institutional Committee on Animal Bioethics and Care (protocol 15-155-M). Animals in this  
36  
37 study were infected by intravenous injection with a single dose of WHV inoculum containing  $6.5$   
38  
39  $\times 10^{10}$  DNase digestion-protected virus copies (also called virion genome equivalents). Animals  
40  
41 were followed by bi-monthly evaluations of serum WHV surface antigen (WHsAg), WHV DNA  
42  
43 and gamma-glutamyl transferase (GGT) levels. Since progressively increasing level of serum  
44  
45 GGT is an indicator of HCC development in woodchucks and GGT levels above 50 IU/L are  
46  
47 indicative of well-established HCC, the animals examined were injected with NPs when GGT  
48  
49 levels achieved values between 61 and 484 IU/L. These animals were followed between 15 and  
50  
51 30 months after injection with WHV. A total of 10 adult woodchucks, 6 chronically infected  
52  
53  
54  
55  
56  
57

1  
2  
3 with WHV and bearing HCC and 4 healthy animals were used of which 7 animals were  
4  
5 examined after 12 h p.i. with NPs and 3 after 48 h p.i. with NPs tested. The animals' hematology  
6  
7 and biochemistry assessments are summarized in Figure S10B. Total blood was estimated as 5%  
8  
9 of total body weight using the lowest measured weight in the previous 12 months to account for  
10  
11 significant seasonal fluctuations in body weight. Woodchuck seasonal weight is mainly a  
12  
13 function of an increase in adipose tissue during fall and is not connected with changes in total  
14  
15 blood volume.  
16  
17  
18  
19  
20

### 21 Synthesis of 60-nm Citrate-Coated Gold Nanoparticles

22  
23 15-nm gold NPs were synthesized by the citrate reduction method described previously.<sup>95</sup> To  
24  
25 make 15-nm particles, 1 mL of 1% (w/v) HAuCl<sub>4</sub> solution was added to 98 mL of ultra-pure  
26  
27 water in a 250 mL Erlenmeyer flask and the mixture was brought to a rapid boil on a stir plate set  
28  
29 to 300°C. One mL of 3% (w/v) Na<sub>3</sub>C<sub>6</sub>H<sub>5</sub>O<sub>7</sub> was then quickly injected under intense stirring and  
30  
31 the mixture was kept on a heated stir plate for 10 min, then cooled on ice, and 15-nm gold NPs  
32  
33 concentration was adjusted to 2.4 nM. Next, 415 mL of ultra-pure water in a 1 L Erlenmeyer  
34  
35 flask, 4.93 mL of 10% (w/v) HAuCl<sub>4</sub> solution, 4.93 mL of 4.4% (w/v) trisodium citrate solution,  
36  
37 4.93 mL of 2.75% (w/v) hydroquinone solution, and 70.5 mL of 2.4 nM 15-nm NPs were all  
38  
39 cooled on ice for 1 hour. The Erlenmeyer flask containing ultra-pure water was then placed in an  
40  
41 ice bath and under intense stirring, the cooled solutions listed above were rapidly injected  
42  
43 sequentially. After overnight stirring, 60-nm gold NPs were purified by centrifugation twice at  
44  
45 1,200 x g using ultra-pure water with 0.05% (v/v) Tween-20 as the resuspension buffer. NPs'  
46  
47 concentration was adjusted to 16 nM.  
48  
49  
50  
51  
52  
53  
54  
55  
56  
57  
58  
59  
60

1  
2  
3 To synthesize fluorescently labeled nanoparticles, 10 mL of 60-nm gold NPs at 15 nM  
4 concentration were reacted with 13.6 mg of amine and thiol terminated 5-kDa polyethylene  
5 glycol (NH<sub>2</sub>-PEG-SH) and 153.8 mg of methoxy and thiol terminated 10-kDa polyethylene  
6 glycol (mPEG-SH). Reactions were incubated at 60°C for 30 min, followed by purification of  
7 resulting nanoparticles by centrifugation 3 times at 1,200 x g in PBS and further reacted with IR  
8 750 NHS ester dye for 1 hour at room temperature. Finally, NPs were purified by centrifugation  
9 as above and resuspended in filtered through 0.22- $\mu$ m membrane PBS at a concentration of 77  
10 mg/mL.  
11  
12  
13  
14  
15  
16  
17  
18  
19  
20  
21  
22

23 Sources of chemicals: IR 750 NHS ester dye was purchased from Fluoroprobes (Scottsdale, AZ,  
24 USA) and Tween-20 from Biobasic (Markham, Ontario, Canada). All other chemicals were  
25 purchased from Sigma-Aldrich.  
26  
27  
28  
29  
30  
31

### 32 *In vivo* Injection of 60-nm Gold Nanoparticles

33  
34  
35 *In vivo* NP experiments were carried out at Memorial University. Briefly, 60-nm gold NPs were  
36 *i.v.* injected into a vein located on the front of the back-leg paws. The dose delivered was 14  
37 mg/kg at a concentration of 77.3 mg/mL. Animals were monitored over the course of 12 or 48  
38 hours. Blood was taken at 4 different time points, *i.e.*,  $t = 0$  minutes, 5 minutes, 4 h, and 12 h *p.i.*,  
39 to assess pharmacokinetics, blood biochemistry and hematology. Over the course of the  
40 experiment we did not observe any measurable signs of toxicity (also see Figure S10B). At 12 h  
41 *p.i.*, animals were euthanized by injection of a mixture of ketamine and rompun (xylazine).  
42 Internal organs, blood, and urine samples were collected, and NP biodistribution was assessed  
43 through ICP-MS and FACS analyses, confocal and electron microscopy, and liver assessed by  
44 histology and immunocytochemistry.  
45  
46  
47  
48  
49  
50  
51  
52  
53  
54  
55  
56  
57

## Woodchuck Organ Tissue Dissociation

Tumor uninvolved woodchuck liver tissue was dissociated as previously described using a 2-step collagenase perfusion.<sup>96</sup> Bulk tissue was dissociated in a 60-mm tissue culture plate in the presence of a pre-warmed mixture of collagenase MA (VitaCyte, 001-2030) and neutral protease (VitaCyte, 003-1000) in 1 X Hanks' balanced salt solution. 4 mL of digestion mixture was added to each tissue fragment which contained 0.1 million units of collagen degrading activity (CDA) and 0.044 million neutral protease units. Tissue was incubated at 37°C for 10 min, and was further minced and incubated for an additional 10 min. Next, 3.7 mL of cell suspension was homogenized *via* a gentleMACS tissue dissociator using built in protocol m\_liver\_03, then filtered through a 70- $\mu$ m filter on ice. Enzymes were further inactivated by adding a 1:1 ratio of 5% fetal bovine serum (FBS) in PBS to the single-cell suspension. Cell viability was assessed using Vi-Cell XR (Beckman) and single cell suspension from liver tumor, tumor margin and non-tumorous tissue, as well as lung, heart, spleen, and bone marrow were prepared for flow cytometry in 1% FBS in PBS.

## Histology

Woodchuck organ tissue was fixed in 10% formalin. Fixed tissue was then prepared using standard protocols for Hematoxylin and Eosin (H&E) and trichrome staining. For IHC identification of CD68 and CD3 -positive cells (Dako A0452), specimens were incubated in the presence of pepsin, washed, and stained with a 1/150 antibody dilution for one hour.

## Multicolor Flow Cytometry

1  
2  
3 Cells were added to polystyrene flow cytometry tubes (Falcon) and centrifuged for 10 min, 400 x  
4  
5 g at 4°C. Cells were then stained for 30 min at 4°C in 1% FBS in PBS with the following  
6  
7 antibodies: 1:50, APC-conjugated anti-human CD14 (Miltenyi, TÜK4), 1:20 FITC-labelled anti-  
8  
9 mouse CD3 (Biolegend,1F4), 1:100 Zombie Aqua Viability Dye (Biolegend). CD14 (Clone:  
10  
11 TUK4) was the antibody employed to identify monocyte/macrophages since we found the  
12  
13 antibody was woodchuck cross-reactive and it was optimized for flow-based assays. Afterwards,  
14  
15 cells were fixed with cytofix/perm (BD) for 15 min at 4°C and washed twice with 1% FBS in  
16  
17 PBS. Finally, stained cells were examined by flow cytometry using an LSRII cytometer (BD).  
18  
19  
20  
21  
22

### 23 Immunofluorescence and Confocal Microscopy

24  
25  
26 Liver non-parenchymal cell (NPC) fraction was enriched by removing hepatocytes from the total  
27  
28 liver cell suspension prepared from the NP-injected healthy and WHV-infected woodchuck liver  
29  
30 *via* centrifugation at 50 x g for 5 min. A CD14<sup>+</sup> cell enrichment was performed on this fraction  
31  
32 by positive selection using magnetic labelling by MACS CD14 microbeads (Miltenyi, 130-050-  
33  
34 201). The cells were fixed in 4% paraformaldehyde, 20 mins, room temperature (RT) and  
35  
36 permeabilized in 0.5% Triton X-100 for 10 mins at RT prior to staining. CD14<sup>+</sup> cells were either  
37  
38 stained for actin conjugated to AF488 (Phalloidin, Catalogue: A12379, Company:  
39  
40 ThermoFisher), or stained with a nuclear stain (2 µg/mL Hoechst 33342 (Catalogue: H3570,  
41  
42 Company: ThermoFisher)) for 1 h at RT, or with FITC-labelled anti-CD14 (Clone: TUK4,  
43  
44 Catalogue: 130-113-146, Company: Miltenyi) antibody at a 1:50 dilution, and nucleus stain at  
45  
46 4°C for 10 mins. Low-melting agarose slides were prepared using 25 µL of 10 mg/mL solution  
47  
48 per slide which were air-dried for 10-20 mins. The slides were prepared by applying the stained  
49  
50 cells resuspended in 20 µL PBS with cover slips on top. Cells were imaged using Nikon A1R  
51  
52 confocal microscope at 40 X objective.  
53  
54  
55  
56  
57

### Electron Microscopy:

For transmission electron microscopy (TEM) experiments, the samples were fixed in 3% glutaraldehyde in 0.1 M Sorenson's phosphate buffer (pH 7.4), rinsed and post-fixed in 1% OsO<sub>4</sub> (Electron Microscopy Sciences) for 1 hour. Following fixation, the tissue was again rinsed with 0.1 M Sorenson's phosphate buffer, dehydrated through an ascending ethanol series, then infiltrated with and embedded in modified Spurr's resin. For the area of interest, identified by thick sectioning, ultrathin sections (90-100 nm) were cut with a Leica UC6 ultramicrotome. Thin sections were stained with uranylless and lead citrate then examined under the Hitachi HT7700 transmission electron microscope. All chemicals were purchased from Sigma Aldrich unless otherwise noted.

For scanning electron microscopy (SEM) experiments, the samples were cut into 2-3mm cubes and fixed in 2.5% glutaraldehyde in PBS. Tissue was washed in 0.1 M Sorenson's Phosphate buffer (pH 7.4), and post-fixed in 1% OsO<sub>4</sub> (Electron Microscopy Sciences) for one hour. After, the tissue was again rinsed with 0.1 M Sorenson's Phosphate buffer, it was dehydrated through an ascending ethanol series and further dried using increasing ratios of HMDS (hexamethyldisilazane) and ethanol. Samples were then left in 100% HMDS overnight to dry completely. The next day they were mounted, sputter coated with gold-palladium with a BAL-TEC SCD 050 Sputter Coater and examined under the Hitachi SU3500 scanning electron microscope.

### Inductive Coupled Plasma Mass Spectrometry (ICP-MS)

1  
2  
3 Organ tissue were collected in 15 mL polypropylene tubes and digested first with 0.8 mL of 16  
4 M nitric acid for 1 hour in water bath at 80C°. Next, 0.2 mL of 12 M hydrochloric acid was  
5 added to each sample and incubated for another hour under the same conditions. Following  
6 digestion, samples were diluted to 40 mL with deionized water for a final acid concentration of  
7 2.5% (v/v). 10 mL of the diluted solution was filtered through a 0.22- $\mu$ M PES filter (Fisher  
8 Scientific SLGP033RS) into a 15 mL tube. Standard curve for elemental gold was prepared with  
9 2% (v/v) nitric acid and 0.5% (v/v) hydrochloric acid beginning with 100 mg/mL and performing  
10 10x dilutions to 0.0001 mg/mL. A reference blank of 0 was also included. Samples were  
11 quantified using NexION 350x ICP-MS (PerkinElmer) with mass analyzer set to gold AU 197.  
12 Carrier solution composed of 2% (v/v) nitric acid and iridium internal standard was mixed with  
13 each sample before injection into the spectrometer. Percent injected dose for each organ was  
14 calculated by multiplying the amount of gold measured per gram of tissue with the total weight  
15 of the organ and then divided by the total measured gold mass in the initial injected dose.  
16  
17  
18  
19  
20  
21  
22  
23  
24  
25  
26  
27  
28  
29  
30  
31  
32

### 33 RNA Extraction and Bulk RNA Sequencing of Sorted Fractions of NP-treated Cells

34  
35  
36  
37 Uninvolved liver homogenate from a NP-treated, WHV-infected, tumor bearing animal was  
38 stained with Live/dead aqua, CD14 and assessed for the expression of CD14 and NP  
39 fluorescence by flow cytometry-based sorting. Four fractions were collected: CD14<sup>+</sup>NP<sup>-</sup>, CD14<sup>-</sup>  
40 NP<sup>-</sup>, CD14<sup>-</sup>NP<sup>+</sup>, and CD14<sup>+</sup>NP<sup>+</sup> (Figure S9A) and 50,000 cells were targeted for each fraction.  
41  
42  
43  
44  
45  
46  
47  
48  
49  
50  
51  
52  
53  
54  
55  
56  
57  
58  
59  
60

1  
2  
3 Experiment 3 (see Figure S10A) was put on dry ice and lysis buffer was added directly to the  
4 pellet to release nucleic acids. Lysate flow-through containing total RNA was proteinase K  
5 treated in the presence of ethanol, bound to a silica gel membrane spin column, purified through  
6 a DNase digest step and ethanol washed before being eluted in 40  $\mu$ L of RNase-free water. Other  
7 deviations from standard protocol included: passing the lysate through the DNA spin column  
8 twice; passing RNA-containing flow-through through the RNA spin column twice; extending  
9 elution incubation time to 5 minutes; extending elution spin time to 2 minutes at max speed;  
10 reloading initial eluent onto the column and repeating elution step to increase RNA  
11 concentration.  
12  
13  
14  
15  
16  
17  
18  
19  
20  
21  
22  
23

#### 24 Illumina RNA Sequencing

25  
26  
27 Library preparation and sequencing: RNA samples were assessed on a RNA 6000 Pico chip  
28 (Agilent Technologies) using the Agilent Bioanalyzer to determine sample RNA integrity  
29 number (RIN) and quantified by the Qubit RNA HS assay kit (Life Technologies). Samples  
30 ranged in RIN values from 8.7 – 9.3. Ten nanograms of sample RNA was used to prepare RNA  
31 libraries using the SMARTer Stranded Total RNA-seq Kit v2 – Pico Input Mammalian (Takara  
32 Bio USA Inc.). Briefly, the samples underwent first-strand synthesis *via* random priming oligos  
33 on the 3'-end. A template switching oligo mix (TSO) was then incorporated to allow the RT  
34 reaction to continue replicating the 5'-end of the RNA strand. Following this, the samples were  
35 PCR amplified to incorporate full-length Illumina adapters and sample barcodes by binding to  
36 either the TSO stretch on the 5'-end, or the random priming oligo sequence on the 3'-end. The  
37 amplified cDNA is treated with ZapR which specifically targets ribosomal RNA in the presence  
38 of mammalian-specific R-Probes. This process leaves non-ribosomal RNA untouched, while  
39 ribosomal RNA are cleaved, leaving them unamplifiable. A final PCR reaction is done to enrich  
40  
41  
42  
43  
44  
45  
46  
47  
48  
49  
50  
51  
52  
53  
54  
55  
56  
57

1  
2  
3 the uncut strands of cDNA to generate the final RNA library. Final RNA library sizing was  
4  
5 verified on the Agilent high sensitivity DNA kit (Agilent Technologies) using the Agilent  
6  
7 Bioanalyzer while library concentration was quantified by qPCR using the KAPA SYBR FAST  
8  
9 qPCR kit (Kapa Biosystems). Libraries were normalized to 10 nM, diluted to 2 nM, denatured  
10  
11 using 0.2 N NaOH, and diluted to a final concentration of 2.2 pM before loading onto the  
12  
13 NextSeq 500 system. The samples were sequenced as a pair-end 150 cycle sequencing run to  
14  
15 achieve a minimum of ~40 M reads per sample.  
16  
17  
18

## 19 RNA-seq Analysis

20  
21  
22  
23 Bulk RNA-seq data from woodchuck was aligned against the alpine marmot genome  
24  
25 (GenBank accession number GCA\_001458135.1). Alignment was carried out using the  
26  
27 following algorithms: STAR Version 2.6A to align the reads and Feature Count (part of the  
28  
29 SUBREAD package) to calculate gene expression count. Edge R and DSeq2 were used to  
30  
31 calculate differentially expressed genes. Data has been deposited in NCBI GEO (GSE147273).  
32  
33 Pathway analysis was also performed and included pathway enrichment analysis examining  
34  
35 active cellular pathways in sorted cell clusters (shown in Figure 6B) which was carried out using  
36  
37 Gene Set Variation Analysis (GSVA) software from Bioconductor (version 1.28).<sup>97</sup> The gene set  
38  
39 Mouse\_GOBP\_AllPathways\_no\_GO\_ia\_July\_05\_2019\_symbol.gmt from  
40  
41 [\[http://baderlab.org/GeneSets\]](http://baderlab.org/GeneSets) was used to identify enriched cellular pathways in GSVA  
42  
43 analysis. Highly related pathways were grouped into a theme and labeled by AutoAnnotate  
44  
45 (version 1.2) in Cytoscape (Version 3.7.2). GSVA results were visualized using the Enrichment  
46  
47 Map app (Version 3.1.0) in Cytoscape (Version 3.7.2).<sup>98</sup> Gene enrichment values expressed in  
48  
49 log<sub>2</sub> are attached in a supplementary excel document (Supplementary Table 2).  
50  
51  
52  
53  
54  
55  
56  
57  
58  
59  
60

## Alignment of Woodchuck and Human Protein Sequence

A total of 41,823 amino acid sequences were identified for woodchuck.<sup>99</sup> We aligned these amino acid sequences (GCA\_901343595.1\_MONAX5\_protein) with the publicly available human protein database (GCF\_000001405.39\_GRCh38.p13\_protein) using BLASTp<sup>7</sup> and determined that 37,411 of the 41,823 (~90%) amino acid sequences from woodchuck aligned with human with a bit-score greater than 50 (See Supplementary Table 1).<sup>100</sup>

## ASSOCIATED CONTENT

Supporting Information. Additional data showing nanoparticle characterization, human and woodchuck protein BLASTp alignment, the impact of nanoparticle uptake on the transcriptional profile of CD14<sup>+</sup> monocytes by bulk RNA seq and associated quality control files are supplied as Supporting Information. This material is available free of charge *via* the Internet at <http://pubs.acs.org>.

## AUTHOR INFORMATION

### Corresponding Authors

\* Tel: +1 4165817442 Email: [s.macparland@utoronto.ca](mailto:s.macparland@utoronto.ca)

\* Tel: +1 416 340-5230 Email: [ian.McGilvray@uhn.ca](mailto:ian.McGilvray@uhn.ca)

\* Tel: +1 709 884 3337 Email: [timich@mun.ca](mailto:timich@mun.ca)

### Author Contributions

1  
2  
3 The manuscript was written through contributions of all authors. All authors have given approval  
4  
5 to the final version of the manuscript.  
6  
7

## 8 ACKNOWLEDGMENTS 9

10 We would like to acknowledge the Canadian Liver Foundation's Team Grant in Hepatocellular  
11  
12 Carcinoma to IDM, TIM, WCWC, SAM, the Toronto General and Western Hospital Foundation  
13  
14 and the Natural Sciences and Engineering Research Council (NSERC) Discovery Grant program  
15  
16 RGPIN-2018-05958 to SAM. LYL has received a graduate student fellowship from the Canadian  
17  
18 Network on Hepatitis C (CanHepC). CanHepC is funded by a joint initiative of the Canadian  
19  
20 Institutes of Health Research (CIHR) (NHC-142832) and the Public Health Agency of Canada  
21  
22 (PHAC). We would like to thank Dr. Tracy McGaha in the Department of Immunology at  
23  
24 University of Toronto for the thoughtful scientific discussions. We would like to thank Joy Qu  
25  
26 for generating illustrations for Figs. 1 and 7. We would like to thank Henry Hong and Audrey  
27  
28 Chong of the Imaging Facility in the Department of Cell and Systems Biology at the University  
29  
30 of Toronto for their technical expertise in the sample preparation and the use of the Hitachi  
31  
32 HT7700 Transmission Electron Microscope.  
33  
34  
35  
36  
37  
38  
39  
40

## 41 REFERENCES 42

- 43 1. El-Serag, H. B., Epidemiology of Viral Hepatitis and Hepatocellular Carcinoma.  
44 *Gastroenterology* **2012**, *142*, 1264-1273.e1.
- 45 2. Michalak, T., The Woodchuck Animal Model of Hepatitis B. *Viral Hepatitis Rev.* **1998**,  
46 *4*, 139-165.
- 47 3. Menne, S.; Cote, P. J., The Woodchuck as an Animal Model for Pathogenesis and  
48 Therapy of Chronic Hepatitis B Virus Infection. *World J. Gastroenterol.* **2007**, *13*, 104-124.
- 49 4. Mulrooney-Cousins, P. M.; Michalak, T. I., Asymptomatic Hepadnaviral Persistence and  
50 Its Consequences in the Woodchuck Model of Occult Hepatitis B Virus Infection. *J Clin Transl*  
51 *Hepatol* **2015**, *3*, 211-219.
- 52 5. Popper, H.; Roth, L.; Purcell, R. H.; Tennant, B. C.; Gerin, J. L., Hepatocarcinogenicity  
53 of the Woodchuck Hepatitis Virus. *Proc. Natl. Acad. Sci. U. S. A.* **1987**, *84*, 866-870.  
54  
55  
56  
57  
58  
59  
60

6. Galibert, F.; Chen, T. N.; Mandart, E., Nucleotide Sequence of a Cloned Woodchuck Hepatitis Virus Genome: Comparison with the Hepatitis B Virus Sequence. *J. Virol.* **1982**, *41*, 51-65.
7. Camacho, C.; Coulouris, G.; Avagyan, V.; Ma, N.; Papadopoulos, J.; Bealer, K.; Madden, T. L., Blast+: Architecture and Applications. *BMC Bioinf.* **2009**, *10*, 421.
8. Korba, B. E.; Cote, P.; Hornbuckle, W.; Schinazi, R.; Gangemi, J. D.; Tennant, B. C.; Gerin, J. L., Enhanced Antiviral Benefit of Combination Therapy with Lamivudine and Alpha Interferon against Whv Replication in Chronic Carrier Woodchucks. *Antivir. Ther.* **2000**, *5*, 95-104.
9. Cullen, J. M.; Li, D. H.; Brown, C.; Eisenberg, E. J.; Cundy, K. C.; Wolfe, J.; Toole, J.; Gibbs, C., Antiviral Efficacy and Pharmacokinetics of Oral Adefovir Dipivoxil in Chronically Woodchuck Hepatitis Virus-Infected Woodchucks. *Antimicrob. Agents Chemother.* **2001**, *45*, 2740-2745.
10. Genovesi, E. V.; Lamb, L.; Medina, I.; Taylor, D.; Seifer, M.; Innaimo, S.; Colonno, R. J.; Standring, D. N.; Clark, J. M., Efficacy of the Carbocyclic 2'-Deoxyguanosine Nucleoside Bms-200475 in the Woodchuck Model of Hepatitis B Virus Infection. *Antimicrob. Agents Chemother.* **1998**, *42*, 3209-3217.
11. Korba, B. E.; Schinazi, R. F.; Cote, P.; Tennant, B. C.; Gerin, J. L., Effect of Oral Administration of Emtricitabine on Woodchuck Hepatitis Virus Replication in Chronically Infected Woodchucks. *Antimicrob. Agents Chemother.* **2000**, *44*, 1757-1760.
12. Bryant, M. L.; Bridges, E. G.; Placidi, L.; Faraj, A.; Loi, A. G.; Pierra, C.; Dukhan, D.; Gosselin, G.; Imbach, J. L.; Hernandez, B.; Juodawlakis, A.; Tennant, B.; Korba, B.; Cote, P.; Marion, P.; Cretton-Scott, E.; Schinazi, R. F.; Sommadossi, J. P., Antiviral L-Nucleosides Specific for Hepatitis B Virus Infection. *Antimicrob. Agents Chemother.* **2001**, *45*, 229-235.
13. Menne, S.; Cote, P. J.; Korba, B. E.; Butler, S. D.; George, A. L.; Tochkov, I. A.; Delaney, W. E. t.; Xiong, S.; Gerin, J. L.; Tennant, B. C., Antiviral Effect of Oral Administration of Tenofovir Disoproxil Fumarate in Woodchucks with Chronic Woodchuck Hepatitis Virus Infection. *Antimicrob. Agents Chemother.* **2005**, *49*, 2720-2728.
14. Mason, W. S.; Cullen, J.; Moraleda, G.; Saputelli, J.; Aldrich, C. E.; Miller, D. S.; Tennant, B.; Frick, L.; Averett, D.; Condreay, L. D.; Jilbert, A. R., Lamivudine Therapy of Whv-Infected Woodchucks. *Virology* **1998**, *245*, 18-32.
15. Li, E.; Lin, L.; Chen, C.-W.; Ou, D.-L., Mouse Models for Immunotherapy in Hepatocellular Carcinoma. *Cancers (Basel)* **2019**, *11*, 1800.
16. Aleksic, K.; Lackner, C.; Geigl, J. B.; Schwarz, M.; Auer, M.; Ulz, P.; Fischer, M.; Trajanoski, Z.; Otte, M.; Speicher, M. R., Evolution of Genomic Instability in Diethylnitrosamine-Induced Hepatocarcinogenesis in Mice. *Hepatology* **2011**, *53*, 895-904.
17. Brown, Z. J.; Heinrich, B.; Greten, T. F., Mouse Models of Hepatocellular Carcinoma: An Overview and Highlights for Immunotherapy Research. *Nat. Rev. Gastroenterol. Hepatol.* **2018**, *15*, 536-554.
18. Chauhan, R.; Churchill, N. D.; Mulrooney-Cousins, P. M.; Michalak, T. I., Initial Sites of Hepadnavirus Integration into Host Genome in Human Hepatocytes and in the Woodchuck Model of Hepatitis B-Associated Hepatocellular Carcinoma. *Oncogenesis* **2017**, *6*, e317-e317.
19. Schachtschneider, K. M.; Schwind, R. M.; Darfour-Oduro, K. A.; De, A. K.; Rund, L. A.; Singh, K.; Principe, D. R.; Guzman, G.; Ray, C. E., Jr.; Ozer, H.; Gaba, R. C.; Schook, L. B., A Validated, Transitional and Translational Porcine Model of Hepatocellular Carcinoma. *Oncotarget* **2017**, *8*, 63620-63634.

20. Schook, L. B.; Collares, T. V.; Hu, W.; Liang, Y.; Rodrigues, F. M.; Rund, L. A.; Schachtschneider, K. M.; Seixas, F. K.; Singh, K.; Wells, K. D.; Walters, E. M.; Prather, R. S.; Counter, C. M., A Genetic Porcine Model of Cancer. *PLoS One* **2015**, *10*, e0128864-e0128864.
21. Rous, P.; Beard, J. W., The Progression to Carcinoma of Virus-Induced Rabbit Papillomas (Shope). *J. Exp Med.* **1935**, *62*, 523-548.
22. Galasko, C. S.; Muckle, D. S., Intrasarcolemmal Proliferation of the Vx2 Carcinoma. *Br. J. Cancer* **1974**, *29*, 59-65.
23. Morris, H. P., Studies on the Development, Biochemistry, and Biology of Experimental Hepatomas. In *Adv. Cancer Res.*, Haddow, A.; Weinhouse, S., Eds. Academic Press: Cambridge, Massachusetts, 1965; Vol. 9, pp 227-302.
24. Novikoff, A. B., A Transplantable Rat Liver Tumor Induced by 4-Dimethylaminoazobenzene. *Cancer Res.* **1957**, *17*, 1010.
25. Gade, T. P. F.; Hunt, S. J.; Harrison, N.; Nadolski, G. J.; Weber, C.; Pickup, S.; Furth, E. E.; Schnall, M. D.; Soulen, M. C.; Celeste Simon, M., Segmental Transarterial Embolization in a Translational Rat Model of Hepatocellular Carcinoma. *J. Vasc. Interv. Radiol.* **2015**, *26*, 1229-1237.
26. Hoshida, Y.; Nijman, S. M. B.; Kobayashi, M.; Chan, J. A.; Brunet, J.-P.; Chiang, D. Y.; Villanueva, A.; Newell, P.; Ikeda, K.; Hashimoto, M.; Watanabe, G.; Gabriel, S.; Friedman, S. L.; Kumada, H.; Llovet, J. M.; Golub, T. R., Integrative Transcriptome Analysis Reveals Common Molecular Subclasses of Human Hepatocellular Carcinoma. *Cancer Res.* **2009**, *69*, 7385-7392.
27. Lee, J.-S.; Chu, I.-S.; Heo, J.; Calvisi, D. F.; Sun, Z.; Roskams, T.; Durnez, A.; Demetris, A. J.; Thorgeirsson, S. S., Classification and Prediction of Survival in Hepatocellular Carcinoma by Gene Expression Profiling. *Hepatology* **2004**, *40*, 667-676.
28. Fletcher, S. P.; Chin, D. J.; Ji, Y.; Iniguez, A. L.; Taillon, B.; Swinney, D. C.; Ravindran, P.; Cheng, D. T.; Bitter, H.; Lopatin, U.; Ma, H.; Klumpp, K.; Menne, S., Transcriptomic Analysis of the Woodchuck Model of Chronic Hepatitis B. *Hepatology* **2012**, *56*, 820-830.
29. Sharpless, N. E.; DePinho, R. A., The Mighty Mouse: Genetically Engineered Mouse Models in Cancer Drug Development. *Nat. Rev. Drug Discovery* **2006**, *5*, 741.
30. Choi, S. Y. C.; Lin, D.; Gout, P. W.; Collins, C. C.; Xu, Y.; Wang, Y., Lessons from Patient-Derived Xenografts for Better *In Vitro* Modeling of Human Cancer. *Adv. Drug Delivery Rev.* **2014**, *79-80*, 222-237.
31. Robinson-Smith, T. M.; Isaacsohn, I.; Mercer, C. A.; Zhou, M.; Van Rooijen, N.; Hussein-zadeh, N.; McFarland-Mancini, M. M.; Drew, A. F., Macrophages Mediate Inflammation-Enhanced Metastasis of Ovarian Tumors in Mice. *Cancer Res.* **2007**, *67*, 5708-16.
32. Chanmee, T.; Ontong, P.; Konno, K.; Itano, N., Tumor-Associated Macrophages as Major Players in the Tumor Microenvironment. *Cancers (Basel)* **2014**, *6*, 1670-90.
33. Altorki, N. K.; Markowitz, G. J.; Gao, D.; Port, J. L.; Saxena, A.; Stiles, B.; McGraw, T.; Mittal, V., The Lung Microenvironment: An Important Regulator of Tumour Growth and Metastasis. *Nat. Rev. Cancer* **2019**, *19*, 9-31.
34. Finak, G.; Bertos, N.; Pepin, F.; Sadekova, S.; Souleimanova, M.; Zhao, H.; Chen, H.; Omeroglu, G.; Meterissian, S.; Omeroglu, A.; Hallett, M.; Park, M., Stromal Gene Expression Predicts Clinical Outcome in Breast Cancer. *Nat. Med.* **2008**, *14*, 518.
35. Li, N.; Babaei-Jadidi, R.; Lorenzi, F.; Spencer-Dene, B.; Clarke, P.; Domingo, E.; Tulchinsky, E.; Vries, R. G. J.; Kerr, D.; Pan, Y.; He, Y.; Bates, D. O.; Tomlinson, I.; Clevers, H.; Nateri, A. S., An Fbxw7-Zeb2 Axis Links Emt and Tumour Microenvironment to Promote Colorectal Cancer Stem Cells and Chemoresistance. *Oncogenesis* **2019**, *8*, 13.

- 1  
2  
3 36. Lin, Y.; Xu, J.; Lan, H., Tumor-Associated Macrophages in Tumor Metastasis:  
4 Biological Roles and Clinical Therapeutic Applications. *J. Hematol. Oncol.* **2019**, *12*, 76.  
5 37. Chen, Y.; Song, Y.; Du, W.; Gong, L.; Chang, H.; Zou, Z., Tumor-Associated  
6 Macrophages: An Accomplice in Solid Tumor Progression. *J. Biomed. Sci.* **2019**, *26*, 78.  
7 38. van der Bij, G. J.; Oosterling, S. J.; Meijer, S.; Beelen, R. H. J.; van Egmond, M., The  
8 Role of Macrophages in Tumor Development. *Cell. Oncol.* **2005**, *27*, 203-213.  
9 39. Herwig, M. C.; Bergstrom, C.; Wells, J. R.; Höller, T.; Grossniklaus, H. E., M2/M1 Ratio  
10 of Tumor Associated Macrophages and Ppar-Gamma Expression in Uveal Melanomas with  
11 Class 1 and Class 2 Molecular Profiles. *Exp. Eye Res.* **2013**, *107*, 52-58.  
12 40. Ohri, C. M.; Shikotra, A.; Green, R. H.; Waller, D. A.; Bradding, P., Macrophages within  
13 Nsclc Tumour Islets Are Predominantly of a Cytotoxic M1 Phenotype Associated with Extended  
14 Survival. *Eur. Respir. J.* **2009**, *33*, 118.  
15 41. Zhang, M.; He, Y.; Sun, X.; Li, Q.; Wang, W.; Zhao, A.; Di, W., A High M1/M2 Ratio of  
16 Tumor-Associated Macrophages Is Associated with Extended Survival in Ovarian Cancer  
17 Patients. *J. Ovarian Res.* **2014**, *7*, 19-19.  
18 42. Schmid, D.; Park, C. G.; Hartl, C. A.; Subedi, N.; Cartwright, A. N.; Puerto, R. B.;  
19 Zheng, Y.; Maiarana, J.; Freeman, G. J.; Wucherpfennig, K. W.; Irvine, D. J.; Goldberg, M. S., T  
20 Cell-Targeting Nanoparticles Focus Delivery of Immunotherapy to Improve Antitumor  
21 Immunity. *Nat. Commun.* **2017**, *8*, 1747.  
22 43. Zhang, L.-x.; Xie, X.-x.; Liu, D.-q.; Xu, Z. P.; Liu, R.-t., Efficient Co-Delivery of Neo-  
23 Epitopes Using Dispersion-Stable Layered Double Hydroxide Nanoparticles for Enhanced  
24 Melanoma Immunotherapy. *Biomaterials* **2018**, *174*, 54-66.  
25 44. Zhang, X.; Tian, W.; Cai, X.; Wang, X.; Dang, W.; Tang, H.; Cao, H.; Wang, L.; Chen,  
26 T., Hydrazinocurcumin Encapsulated Nanoparticles “Re-Educate” Tumor-Associated  
27 Macrophages and Exhibit Anti-Tumor Effects on Breast Cancer Following Stat3 Suppression.  
28 *PLoS One* **2013**, *8*, e65896.  
29 45. Shi, C.; Liu, T.; Guo, Z.; Zhuang, R.; Zhang, X.; Chen, X., Reprogramming Tumor-  
30 Associated Macrophages by Nanoparticle-Based Reactive Oxygen Species Photogeneration.  
31 *Nano Lett.* **2018**, *18*, 7330-7342.  
32 46. Rojas, J. M.; Sanz-Ortega, L.; Mulens-Arias, V.; Gutiérrez, L.; Pérez-Yagüe, S.; Barber,  
33 D. F., Superparamagnetic Iron Oxide Nanoparticle Uptake Alters M2 Macrophage Phenotype,  
34 Iron Metabolism, Migration and Invasion. *Nanomedicine* **2016**, *12*, 1127-1138.  
35 47. Bareford, M. D.; Hamed, H. A.; Tang, Y.; Cruickshanks, N.; Burow, M. E.; Fisher, P. B.;  
36 Moran, R. G.; Nephew, K. P.; Grant, S.; Dent, P., Sorafenib Enhances Pemetrexed Cytotoxicity  
37 through an Autophagy-Dependent Mechanism in Cancer Cells. *Autophagy* **2011**, *7*, 1261-1262.  
38 48. Zhu, Y.-j.; Zheng, B.; Wang, H.-y.; Chen, L., New Knowledge of the Mechanisms of  
39 Sorafenib Resistance in Liver Cancer. *Acta Pharmacol. Sin.* **2017**, *38*, 614-622.  
40 49. Elia, A. R.; Grioni, M.; Basso, V.; Curnis, F.; Freschi, M.; Corti, A.; Mondino, A.;  
41 Bellone, M., Targeting Tumor Vasculature with Tnf Leads Effector T Cells to the Tumor and  
42 Enhances Therapeutic Efficacy of Immune Checkpoint Blockers in Combination with Adoptive  
43 Cell Therapy. *Clin. Cancer Res.* **2018**, *24*, 2171.  
44 50. Schaaf, M. B.; Garg, A. D.; Agostinis, P., Defining the Role of the Tumor Vasculature in  
45 Antitumor Immunity and Immunotherapy. *Cell Death Dis.* **2018**, *9*, 115.  
46 51. Murphy, E. A.; Majeti, B. K.; Barnes, L. A.; Makale, M.; Weis, S. M.; Lutu-Fuga, K.;  
47 Wrasidlo, W.; Cheresch, D. A., Nanoparticle-Mediated Drug Delivery to Tumor Vasculature  
48 Suppresses Metastasis. *Proc. Natl. Acad. Sci. U. S. A.* **2008**, *105*, 9343.  
49  
50  
51  
52  
53  
54  
55  
56  
57  
58  
59  
60

- 1  
2  
3 52. Dvorak, H. F.; Nagy, J. A.; Dvorak, J. T.; Dvorak, A. M., Identification and  
4 Characterization of the Blood Vessels of Solid Tumors That Are Leaky to Circulating  
5 Macromolecules. *Am. J. Pathol.* **1988**, *133*, 95-109.
- 6 53. Ekdawi, S. N.; Stewart, J. M. P.; Dunne, M.; Stapleton, S.; Mitsakakis, N.; Dou, Y. N.;  
7 Jaffray, D. A.; Allen, C., Spatial and Temporal Mapping of Heterogeneity in Liposome Uptake  
8 and Microvascular Distribution in an Orthotopic Tumor Xenograft Model. *J. Controlled Release*  
9 **2015**, *207*, 101-111.
- 10 54. Balasubramanian, S. K.; Jittiwat, J.; Manikandan, J.; Ong, C.-N.; Yu, L. E.; Ong, W.-Y.,  
11 Biodistribution of Gold Nanoparticles and Gene Expression Changes in the Liver and Spleen  
12 after Intravenous Administration in Rats. *Biomaterials* **2010**, *31*, 2034-2042.
- 13 55. Lipka, J.; Semmler-Behnke, M.; Sperling, R. A.; Wenk, A.; Takenaka, S.; Schleh, C.;  
14 Kissel, T.; Parak, W. J.; Kreyling, W. G., Biodistribution of Peg-Modified Gold Nanoparticles  
15 Following Intratracheal Instillation and Intravenous Injection. *Biomaterials* **2010**, *31*, 6574-6581.
- 16 56. Elci, S. G.; Jiang, Y.; Yan, B.; Kim, S. T.; Saha, K.; Moyano, D. F.; Yesilbag Tonga, G.;  
17 Jackson, L. C.; Rotello, V. M.; Vachet, R. W., Surface Charge Controls the Suborgan  
18 Biodistributions of Gold Nanoparticles. *ACS Nano* **2016**, *10*, 5536-5542.
- 19 57. Yang, L.; Kuang, H.; Zhang, W.; Aguilar, Z. P.; Wei, H.; Xu, H., Comparisons of the  
20 Biodistribution and Toxicological Examinations after Repeated Intravenous Administration of  
21 Silver and Gold Nanoparticles in Mice. *Sci. Rep.* **2017**, *7*, 3303.
- 22 58. Ma, X.; Wu, Y.; Jin, S.; Tian, Y.; Zhang, X.; Zhao, Y.; Yu, L.; Liang, X.-J., Gold  
23 Nanoparticles Induce Autophagosome Accumulation through Size-Dependent Nanoparticle  
24 Uptake and Lysosome Impairment. *ACS Nano* **2011**, *5*, 8629-8639.
- 25 59. Sindhvani, S.; Syed, A. M.; Ngai, J.; Kingston, B. R.; Maiorino, L.; Rothschild, J.;  
26 MacMillan, P.; Zhang, Y.; Rajesh, N. U.; Hoang, T.; Wu, J. L. Y.; Wilhelm, S.; Zilman, A.;  
27 Gadde, S.; Sulaiman, A.; Ouyang, B.; Lin, Z.; Wang, L.; Egeblad, M.; Chan, W. C. W., The  
28 Entry of Nanoparticles into Solid Tumours. *Nat. Mater.* **2020**.
- 29 60. Perrault, S. D.; Walkey, C.; Jennings, T.; Fischer, H. C.; Chan, W. C. W., Mediating  
30 Tumor Targeting Efficiency of Nanoparticles through Design. *Nano Lett.* **2009**, *9*, 1909-1915.
- 31 61. Sykes, E. A.; Chen, J.; Zheng, G.; Chan, W. C. W., Investigating the Impact of  
32 Nanoparticle Size on Active and Passive Tumor Targeting Efficiency. *ACS Nano* **2014**, *8*, 5696-  
33 5706.
- 34 62. Sykes, E. A.; Dai, Q.; Sarsons, C. D.; Chen, J.; Rocheleau, J. V.; Hwang, D. M.; Zheng,  
35 G.; Cramb, D. T.; Rinker, K. D.; Chan, W. C. W., Tailoring Nanoparticle Designs to Target  
36 Cancer Based on Tumor Pathophysiology. *Proc. Natl. Acad. Sci. U. S. A.* **2016**, *113*, E1142.
- 37 63. Lunov, O.; Syrovets, T.; Loos, C.; Beil, J.; Delacher, M.; Tron, K.; Nienhaus, G. U.;  
38 Musyanovych, A.; Mailänder, V.; Landfester, K.; Simmet, T., Differential Uptake of  
39 Functionalized Polystyrene Nanoparticles by Human Macrophages and a Monocytic Cell Line.  
40 *ACS Nano* **2011**, *5*, 1657-1669.
- 41 64. Arvizo, R. R.; Miranda, O. R.; Thompson, M. A.; Pabelick, C. M.; Bhattacharya, R.;  
42 Robertson, J. D.; Rotello, V. M.; Prakash, Y. S.; Mukherjee, P., Effect of Nanoparticle Surface  
43 Charge at the Plasma Membrane and Beyond. *Nano Lett.* **2010**, *10*, 2543-2548.
- 44 65. Sonavane, G.; Tomoda, K.; Makino, K., Biodistribution of Colloidal Gold Nanoparticles  
45 after Intravenous Administration: Effect of Particle Size. *Colloids Surf., B* **2008**, *66*, 274-280.
- 46 66. Soo Choi, H.; Liu, W.; Misra, P.; Tanaka, E.; Zimmer, J. P.; Itty Ipe, B.; Bawendi, M. G.;  
47 Frangioni, J. V., Renal Clearance of Quantum Dots. *Nat. Biotechnol.* **2007**, *25*, 1165-1170.
- 48 67. Poon, W.; Zhang, Y.-N.; Ouyang, B.; Kingston, B. R.; Wu, J. L. Y.; Wilhelm, S.; Chan,  
49 W. C. W., Elimination Pathways of Nanoparticles. *ACS Nano* **2019**, *13*, 5785-5798.
- 50  
51  
52  
53  
54  
55  
56  
57  
58  
59  
60

- 1  
2  
3 68. MacParland, S. A.; Tsoi, K. M.; Ouyang, B.; Ma, X. Z.; Manuel, J.; Fawaz, A.;  
4 Ostrowski, M. A.; Alman, B. A.; Zilman, A.; Chan, W. C.; McGilvray, I. D., Phenotype  
5 Determines Nanoparticle Uptake by Human Macrophages from Liver and Blood. *ACS Nano*  
6 **2017**, *11*, 2428-2443.
- 7 69. Goodrich, G.; Bao, L.; Gill-Sharp, K.; Sang, K.; Wang, J.; Payne, J. D., Photothermal  
8 Therapy in a Murine Colon Cancer Model Using Near-Infrared Absorbing Gold Nanorods. *J.*  
9 *Biomed. Opt.* **2010**, *15*, 018001.
- 10 70. Popper, H., Injury and Repair of Liver Cells. *Med. Clin. North Am.* **1979**, *63*, 479-493.
- 11 71. Xu, P.; Van Kirk, E. A.; Murdoch, W. J.; Zhan, Y.; Isaak, D. D.; Radosz, M.; Shen, Y.,  
12 Anticancer Efficacies of Cisplatin-Releasing Ph-Responsive Nanoparticles. *Biomacromolecules*  
13 **2006**, *7*, 829-835.
- 14 72. Lv, Y.; Hao, L.; Hu, W.; Ran, Y.; Bai, Y.; Zhang, L., Novel Multifunctional Ph-Sensitive  
15 Nanoparticles Loaded into Microbubbles as Drug Delivery Vehicles for Enhanced Tumor  
16 Targeting. *Sci. Rep.* **2016**, *6*, 29321.
- 17 73. Zhu, J.; He, K.; Dai, Z.; Gong, L.; Zhou, T.; Liang, H.; Liu, J., Self-Assembly of  
18 Luminescent Gold Nanoparticles with Sensitive Ph-Stimulated Structure Transformation and  
19 Emission Response toward Lysosome Escape and Intracellular Imaging. *Anal. Chem.* **2019**.
- 20 74. Goldacre, R. J.; Sylven, B., On the Access of Blood-Borne Dyes to Various Tumour  
21 Regions. *Br. J. Cancer* **1962**, *16*, 306-322.
- 22 75. El Emir, E.; Qureshi, U.; Dearling, J. L. J.; Boxer, G. M.; Clatworthy, I.; Folarin, A. A.;  
23 Robson, M. P.; Nagl, S.; Konerding, M. A.; Pedley, R. B., Predicting Response to  
24 Radioimmunotherapy from the Tumor Microenvironment of Colorectal Carcinomas. *Cancer*  
25 *Res.* **2007**, *67*, 11896.
- 26 76. Lind, P. A.; Naucler, G.; Holm, A.; Gubanski, M.; Svensson, C., Efficacy of Pegylated  
27 Liposomal Doxorubicin in Patients with Advanced Hepatocellular Carcinoma. *Acta Oncol.* **2007**,  
28 *46*, 230-3.
- 29 77. Zanganeh, S.; Hutter, G.; Spitler, R.; Lenkov, O.; Mahmoudi, M.; Shaw, A.; Pajarinen, J.  
30 S.; Nejadnik, H.; Goodman, S.; Moseley, M.; Coussens, L. M.; Daldrup-Link, H. E., Iron Oxide  
31 Nanoparticles Inhibit Tumour Growth by Inducing Pro-Inflammatory Macrophage Polarization  
32 in Tumour Tissues. *Nat. Nanotechnol.* **2016**, *11*, 986-994.
- 33 78. Su, L.; Zhang, W.; Wu, X.; Zhang, Y.; Chen, X.; Liu, G.; Chen, G.; Jiang, M.,  
34 Glycocalyx-Mimicking Nanoparticles for Stimulation and Polarization of Macrophages *via*  
35 Specific Interactions. *Small* **2015**, *11*, 4191-4200.
- 36 79. Wang, Y.; Lin, Y.-X.; Qiao, S.-L.; An, H.-W.; Ma, Y.; Qiao, Z.-Y.; Rajapaksha, R. P. Y.  
37 J.; Wang, H., Polymeric Nanoparticles Promote Macrophage Reversal from M2 to M1  
38 Phenotypes in the Tumor Microenvironment. *Biomaterials* **2017**, *112*, 153-163.
- 39 80. Miller, M. A.; Zheng, Y.-R.; Gadde, S.; Pfirschke, C.; Zope, H.; Engblom, C.; Kohler, R.  
40 H.; Iwamoto, Y.; Yang, K. S.; Askevold, B.; Kolishetti, N.; Pittet, M.; Lippard, S. J.; Farokhzad,  
41 O. C.; Weissleder, R., Tumour-Associated Macrophages Act as a Slow-Release Reservoir of  
42 Nano-Therapeutic Pt(IV) Pro-Drug. *Nat. Commun.* **2015**, *6*, 8692-8692.
- 43 81. Rose, A. A. N.; Grosset, A.-A.; Dong, Z.; Russo, C.; MacDonald, P. A.; Bertos, N. R.;  
44 St-Pierre, Y.; Simantov, R.; Hallett, M.; Park, M.; Gaboury, L.; Siegel, P. M., Glycoprotein  
45 Nonmetastatic B Is an Independent Prognostic Indicator of Recurrence and a Novel Therapeutic  
46 Target in Breast Cancer. *Clin. Cancer Res.* **2010**, *16*, 2147.
- 47 82. Kobayashi, M.; Chung, J.-S.; Beg, M.; Arriaga, Y.; Verma, U.; Courtney, K.; Mansour,  
48 J.; Haley, B.; Khan, S.; Horiuchi, Y.; Ramani, V.; Harker, D.; Gopal, P.; Araghizadeh, F.; Cruz,  
49 P. D.; Ariizumi, K., Blocking Monocytic Myeloid-Derived Suppressor Cell Function *via* Anti-  
50  
51  
52  
53  
54  
55  
56  
57  
58  
59  
60

1  
2  
3 Dc-Hil/Gpmb Antibody Restores the <math>In Vitro</math> Integrity of T Cells  
4 from Cancer Patients. *Clin. Cancer Res.* **2019**, *25*, 828.

5 83. Chung, J.-S.; Sato, K.; Dougherty, I. I.; Cruz, P. D.; Ariizumi, K., Dc-Hil Is a Negative  
6 Regulator of T Lymphocyte Activation. *Blood* **2007**, *109*, 4320.

7 84. Tomita, M.; Yamamoto, K.; Kobashi, H.; Ohmoto, M.; Tsuji, T., Immunohistochemical  
8 Phenotyping of Liver Macrophages in Normal and Diseased Human Liver. *Hepatology* **1994**, *20*,  
9 317-325.

10 85. McGuinness, P. H.; Painter, D.; Davies, S.; McCaughan, G. W., Increases in Intrahepatic  
11 Cd68 Positive Cells, Mac387 Positive Cells, and Proinflammatory Cytokines (Particularly  
12 Interleukin 18) in Chronic Hepatitis C Infection. *Gut* **2000**, *46*, 260-269.

13 86. Soulas, C.; Conerly, C.; Kim, W.-K.; Burdo, T. H.; Alvarez, X.; Lackner, A. A.;  
14 Williams, K. C., Recently Infiltrating Mac387(+) Monocytes/Macrophages a Third Macrophage  
15 Population Involved in SIV and HIV Encephalitic Lesion Formation. *Am. J. Pathol.* **2011**, *178*,  
16 2121-2135.

17 87. Antoniadou, C. G.; Quaglia, A.; Taams, L. S.; Mitry, R. R.; Hussain, M.; Abeles, R.;  
18 Possamai, L. A.; Bruce, M.; McPhail, M.; Starling, C.; Wagner, B.; Barnardo, A.; Pomplun, S.;  
19 Auzinger, G.; Bernal, W.; Heaton, N.; Vergani, D.; Thursz, M. R.; Wendon, J., Source and  
20 Characterization of Hepatic Macrophages in Acetaminophen-Induced Acute Liver Failure in  
21 Humans. *Hepatology* **2012**, *56*, 735-746.

22 88. Newman, A. M.; Liu, C. L.; Green, M. R.; Gentles, A. J.; Feng, W.; Xu, Y.; Hoang, C.  
23 D.; Diehn, M.; Alizadeh, A. A., Robust Enumeration of Cell Subsets from Tissue Expression  
24 Profiles. *Nat. Methods* **2015**, *12*, 453.

25 89. Tsoi, K. M.; MacParland, S. A.; Ma, X.-Z.; Spetzler, V. N.; Echeverri, J.; Ouyang, B.;  
26 Fadel, S. M.; Sykes, E. A.; Goldaracena, N.; Kathis, J. M.; Conneely, J. B.; Alman, B. A.;  
27 Selzner, M.; Ostrowski, M. A.; Adeyi, O. A.; Zilman, A.; McGilvray, I. D.; Chan, W. C. W.,  
28 Mechanism of Hard-Nanomaterial Clearance by the Liver. *Nat. Mater.* **2016**, *15*, 1212-1221.

29 90. Manolova, V.; Flace, A.; Bauer, M.; Schwarz, K.; Saudan, P.; Bachmann, M. F.,  
30 Nanoparticles Target Distinct Dendritic Cell Populations According to Their Size. *Eur. J.*  
31 *Immunol.* **2008**, *38*, 1404-1413.

32 91. Rodell, C. B.; Arlauckas, S. P.; Cuccarese, M. F.; Garris, C. S.; Li, R.; Ahmed, M. S.;  
33 Kohler, R. H.; Pittet, M. J.; Weissleder, R., Tlr7/8-Agonist-Loaded Nanoparticles Promote the  
34 Polarization of Tumour-Associated Macrophages to Enhance Cancer Immunotherapy. *Nat.*  
35 *Biomed. Eng.* **2018**, *2*, 578-588.

36 92. Hirahara, K.; Ghoreschi, K.; Yang, X.-P.; Takahashi, H.; Laurence, A.; Vahedi, G.;  
37 Sciumè, G.; Hall, Aisling O. H.; Dupont, Christopher D.; Francisco, Loise M.; Chen, Q.; Tanaka,  
38 M.; Kanno, Y.; Sun, H.-W.; Sharpe, Arlene H.; Hunter, Christopher A.; O'Shea, John J.,  
39 Interleukin-27 Priming of T Cells Controls IL-17 Production in Trans *via* Induction of the Ligand  
40 Pd-L1. *Immunity* **2012**, *36*, 1017-1030.

41 93. Villarino, A. V.; Stumhofer, J. S.; Saris, C. J. M.; Kastelein, R. A.; de Sauvage, F. J.;  
42 Hunter, C. A., IL-27 Limits IL-2 Production During Th1 Differentiation. *J. Immunol.* **2006**, *176*,  
43 237.

44 94. Hu, Z.-Q.; Zhou, S.-L.; Zhou, Z.-J.; Luo, C.-B.; Chen, E.-B.; Zhan, H.; Wang, P.-C.; Dai,  
45 Z.; Zhou, J.; Fan, J.; Huang, X.-W., Overexpression of Semaphorin 3a Promotes Tumor  
46 Progression and Predicts Poor Prognosis in Hepatocellular Carcinoma after Curative Resection.  
47 *Oncotarget* **2016**, *7*, 51733-51746.

48 95. Turkevich, J.; Stevenson, P. C.; Hillier, J., A Study of the Nucleation and Growth  
49 Processes in the Synthesis of Colloidal Gold. *Discuss. Faraday Soc.* **1951**, *11*, 55-75.

- 1  
2  
3 96. MacParland, S. A.; Liu, J. C.; Ma, X.-Z.; Innes, B. T.; Bartczak, A. M.; Gage, B. K.;  
4 Manuel, J.; Khuu, N.; Echeverri, J.; Linares, I.; Gupta, R.; Cheng, M. L.; Liu, L. Y.; Camat, D.;  
5 Chung, S. W.; Seliga, R. K.; Shao, Z.; Lee, E.; Ogawa, S.; Ogawa, M., *et al.*, Single Cell RNA  
6 Sequencing of Human Liver Reveals Distinct Intrahepatic Macrophage Populations. *Nat.*  
7 *Commun.* **2018**, *9*, 4383-4383.
- 8 97. Hänzelmann, S.; Castelo, R.; Guinney, J., Gsva: Gene Set Variation Analysis for  
9 Microarray and RNA-Seq Data. *BMC Bioinf.* **2013**, *14*, 7.
- 10 98. Merico, D.; Isserlin, R.; Stueker, O.; Emili, A.; Bader, G. D., Enrichment Map: A  
11 Network-Based Method for Gene-Set Enrichment Visualization and Interpretation. *PLoS One*  
12 **2010**, *5*, e13984-e13984.
- 13 99. Alioto, T. S.; Cruz, F.; Gomez-Garrido, J.; Triyatni, M.; Gut, M.; Frias, L.; Esteve-  
14 Codina, A.; Menne, S.; Kiialainen, A.; Kumpesa, N.; Birzele, F.; Schmucki, R.; Gut, I. G.;  
15 Spleiss, O., The Genome Sequence of the Eastern Woodchuck (*Marmota Monax*) - A Preclinical  
16 Animal Model for Chronic Hepatitis B. *G3: Genes, Genomes, Genet.* **2019**, *9*, 3943-3952.
- 17 100. Pearson, W. R., An Introduction to Sequence Similarity ("Homology") Searching. *Curr.*  
18 *Protoc. Bioinf.* **2013**, *42*, Unit 3.1.  
19  
20  
21  
22  
23  
24  
25  
26  
27  
28  
29  
30  
31  
32  
33  
34  
35  
36  
37  
38  
39  
40  
41  
42  
43  
44  
45  
46  
47  
48  
49  
50  
51  
52  
53  
54  
55  
56  
57  
58  
59  
60

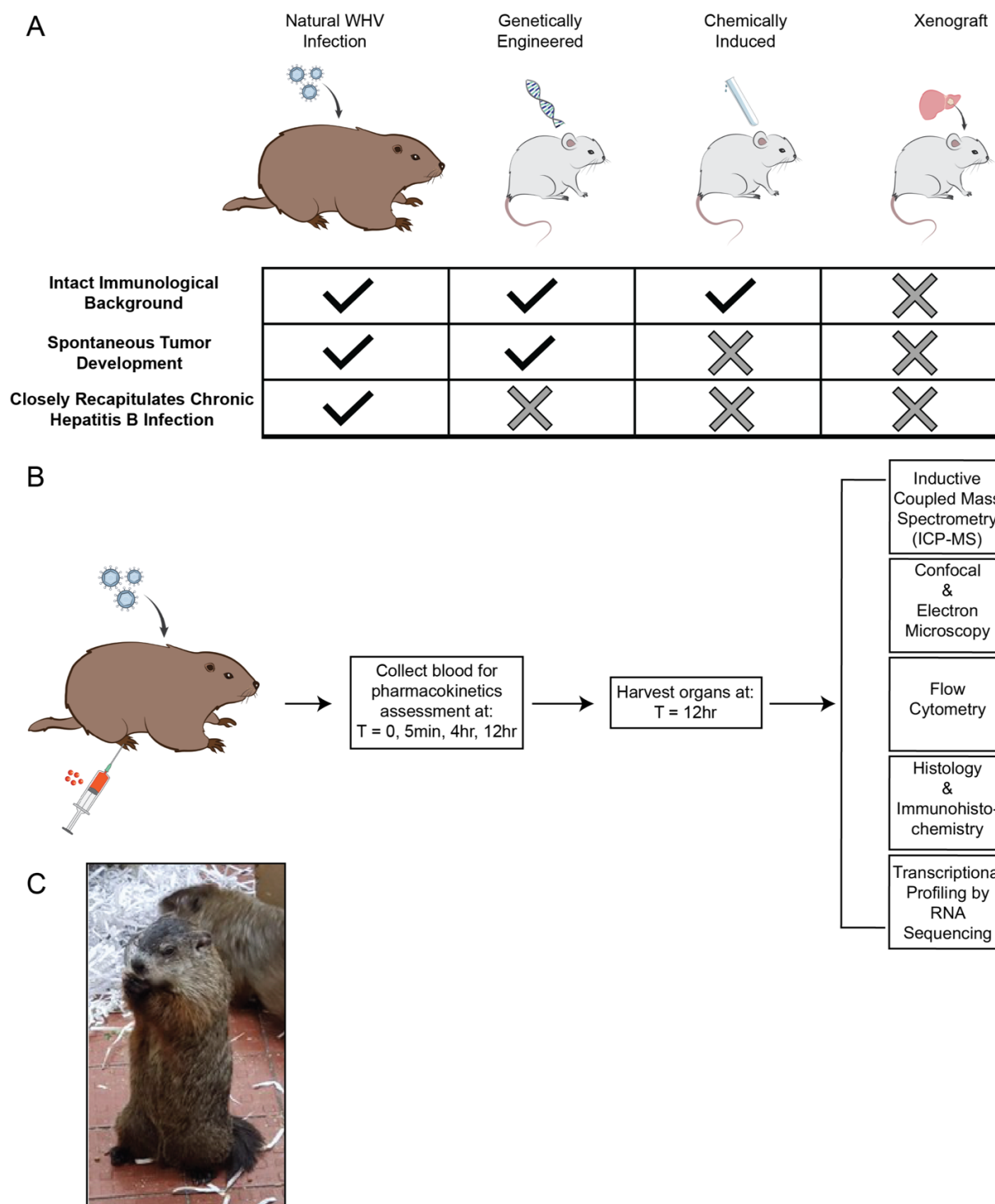
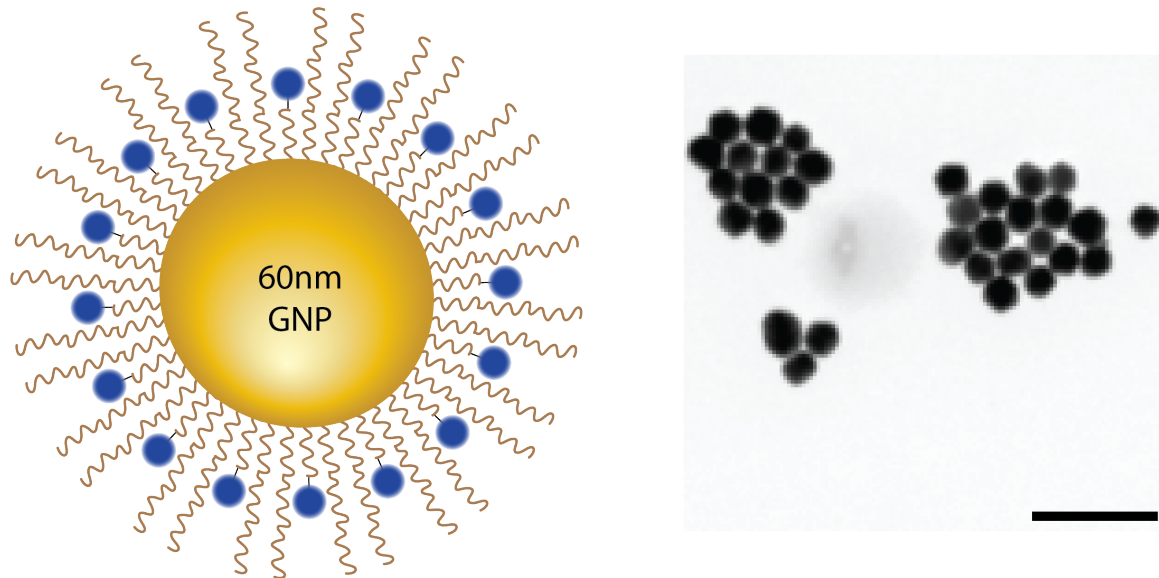


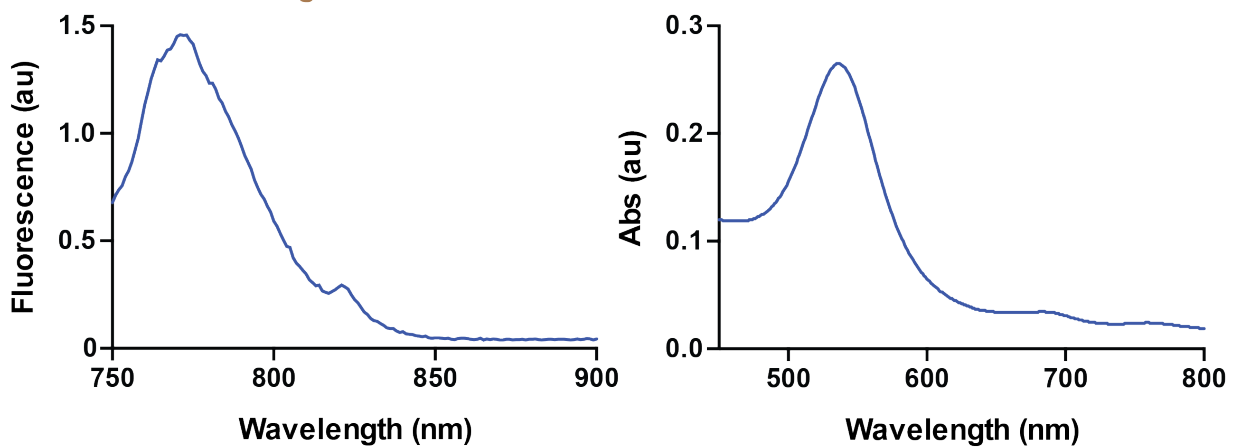
**Figure 1: Summary of *in vivo* tumor models and general experimental workflow.**

(A) Comparison of the woodchuck hepatitis-induced HCC model and other available *in vivo* tumor models used to study hepatocellular carcinoma. (B) Experimental outline showing downstream analysis after intravenous injection of nanoparticles. (C) Original image of adult woodchucks that were employed in this model. Illustrations of woodchucks and mice were designed by Joy Qu.

A

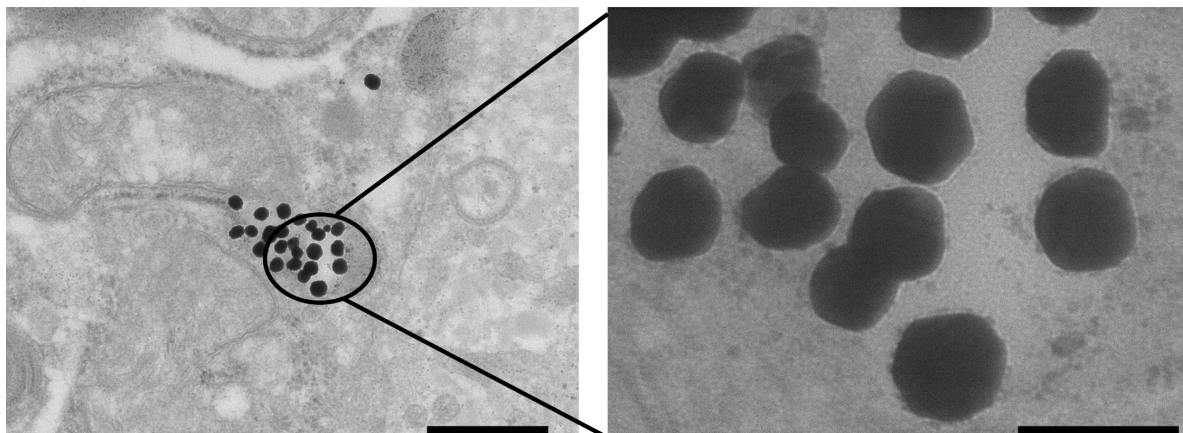


B

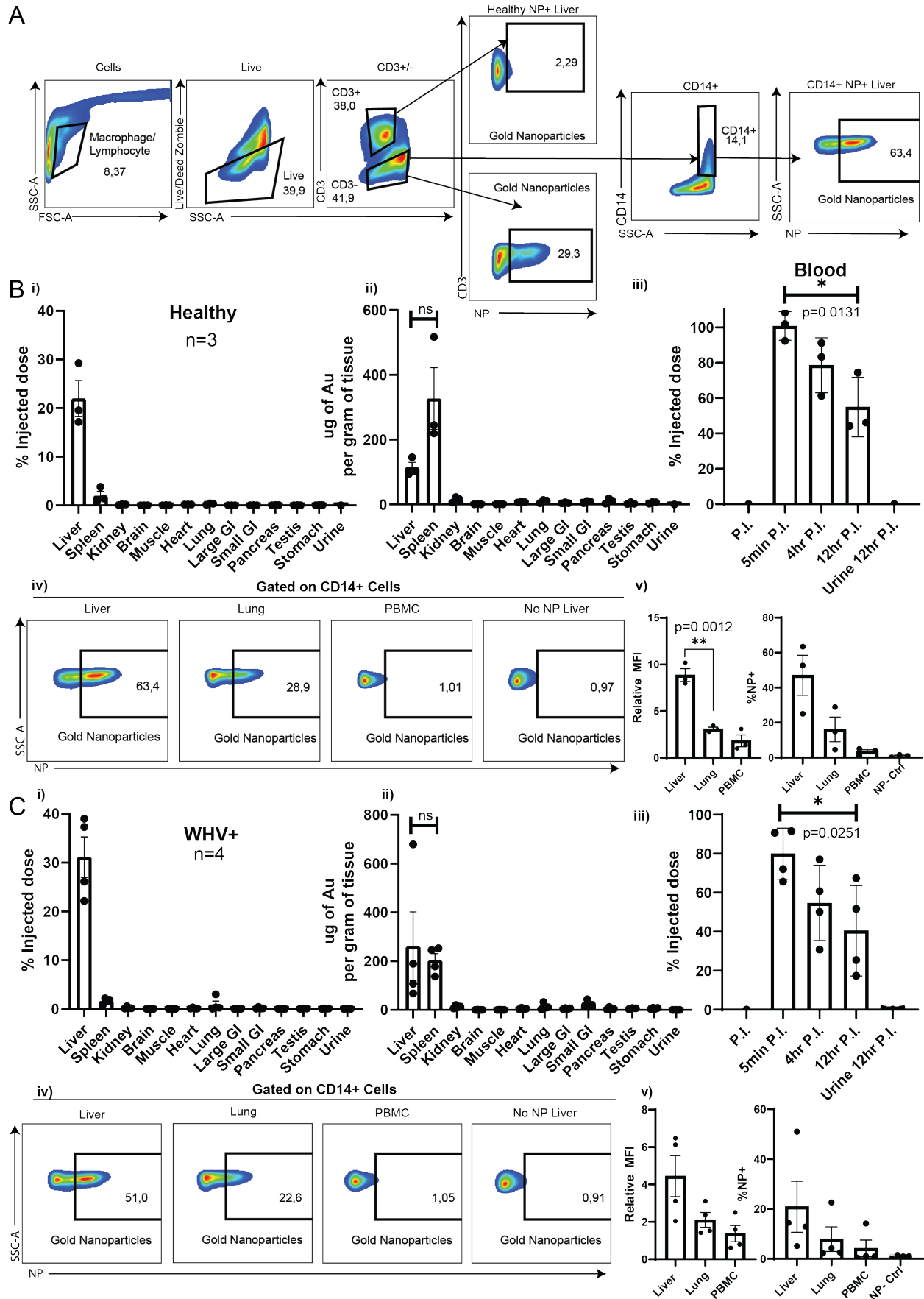


Core Size	Z-Average(HD)	PDI	Z-Potential
60 nm	103.6 nm	0.042	-4.0 (+/-0.4) mV

C



1  
2  
3 **Figure 2: Gold nanoparticle characterization.** (A) Schematic (left) and transmission electron  
4 microscopy (right) of 60-nm gold nanoparticles used for *in vivo* injection experiments. Scale bar  
5 represents 250 nm. (B) Fluorescence and emission wavelengths of NPs. Hydrodynamic size  
6 (HD) is measured by dynamic light scattering (DLS) and cumulants analysis was used to  
7 determine the indicated Z-Average and polydispersity index (PDI). (C) Transmission electron  
8 microscopy of 60-nm gold NPs in woodchuck liver highlighting that the particles remain intact  
9 *in vivo*. Scale bars represents 500 nm (left) and 100 nm (right).  
10  
11  
12  
13  
14  
15  
16  
17  
18  
19  
20  
21  
22  
23  
24  
25  
26  
27  
28  
29  
30  
31  
32  
33  
34  
35  
36  
37  
38  
39  
40  
41  
42  
43  
44  
45  
46  
47  
48  
49  
50  
51  
52  
53  
54  
55  
56  
57  
58  
59  
60



1  
2  
3 **Figure 3: Biodistribution of 60-nm gold nanoparticles in WHV-positive and healthy,**  
4 **uninfected woodchucks.** (A) Gating strategy to assess uptake of NPs in CD3<sup>+</sup> and CD3<sup>-</sup> cell  
5 populations in healthy and WHV-infected animals. NP gates were determined based on FMO  
6 stained samples from animals not injected with NPs. The CD3<sup>-</sup> cell population was subsequently  
7 used to identify CD14<sup>+</sup> and NP<sup>+</sup> cells in liver, lung, and PBMCs. (B) Inductive coupled mass  
8 spectrometry (ICP-MS) was used to assess biodistribution of gold NPs in different organs (i&ii)  
9 and blood (iii). Values are presented as percentage of total injected dose. (iv) Comparative  
10 analysis of CD14<sup>+</sup>NP<sup>+</sup> cells in different organs (liver, lung) and PBMCs by flow cytometry  
11 compared to no NP-treated liver control with relative MFI and percentage of NP<sup>+</sup>CD14<sup>+</sup> cells  
12 from all healthy animals shown graphically (v). (Ci-v) Identical analysis as in (Bi-v) but for  
13 WHV-positive animals. Error bars are representative of at least 3 experiments  $\pm$  SEM. Statistical  
14 significance was evaluated using unpaired t test where (\*) < 0.05, (\*\*) < 0.01 and not significant  
15 (ns). For Bv and Cv, comparisons between organs and PBMC are not significant (p<0.05) unless  
16 stated otherwise.  
17  
18  
19  
20  
21  
22  
23  
24  
25  
26  
27  
28  
29  
30  
31  
32  
33  
34  
35  
36  
37  
38  
39  
40  
41  
42  
43  
44  
45  
46  
47  
48  
49  
50  
51  
52  
53  
54  
55  
56  
57  
58  
59  
60

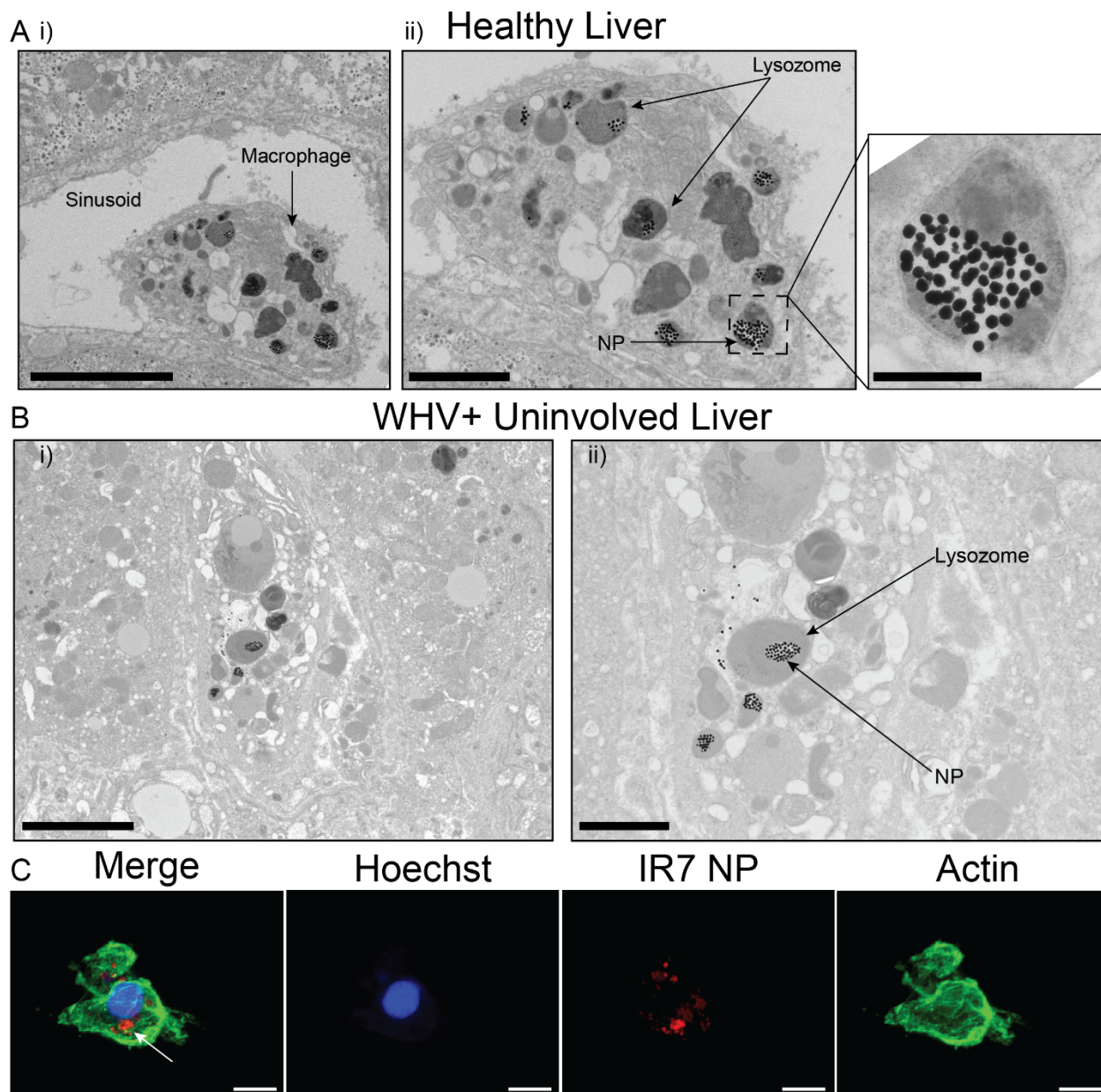


**Figure 4: Electron and confocal microscopy of macrophages from healthy and WHV-infected liver.** (A) Transmission electron microscopy of NP-positive macrophage in sinusoid of healthy woodchuck liver. Subcellular localization of NPs are indicated with black arrows in (ii) and insert. Scale bar represent (i) 5  $\mu\text{m}$  (ii) 2  $\mu\text{m}$  and 500 nm in insert. (B) Same as (A) but in tumor uninvolved liver tissue from a WHV-infected animal. Scale bars represent (i) 5  $\mu\text{m}$  and (ii) 2  $\mu\text{m}$ . (C) Confocal imaging of magnetically sorted CD14<sup>+</sup> cells obtained after enzymatic digestion of uninfected healthy liver tissue. NPs are indicated with white arrow in merge photo. Fluorophores Hoechst, infrared 7 (IR7), and phalloidin stain the nucleus, NPs, and actin, respectively. Scale bars (white) denote 10  $\mu\text{m}$ .

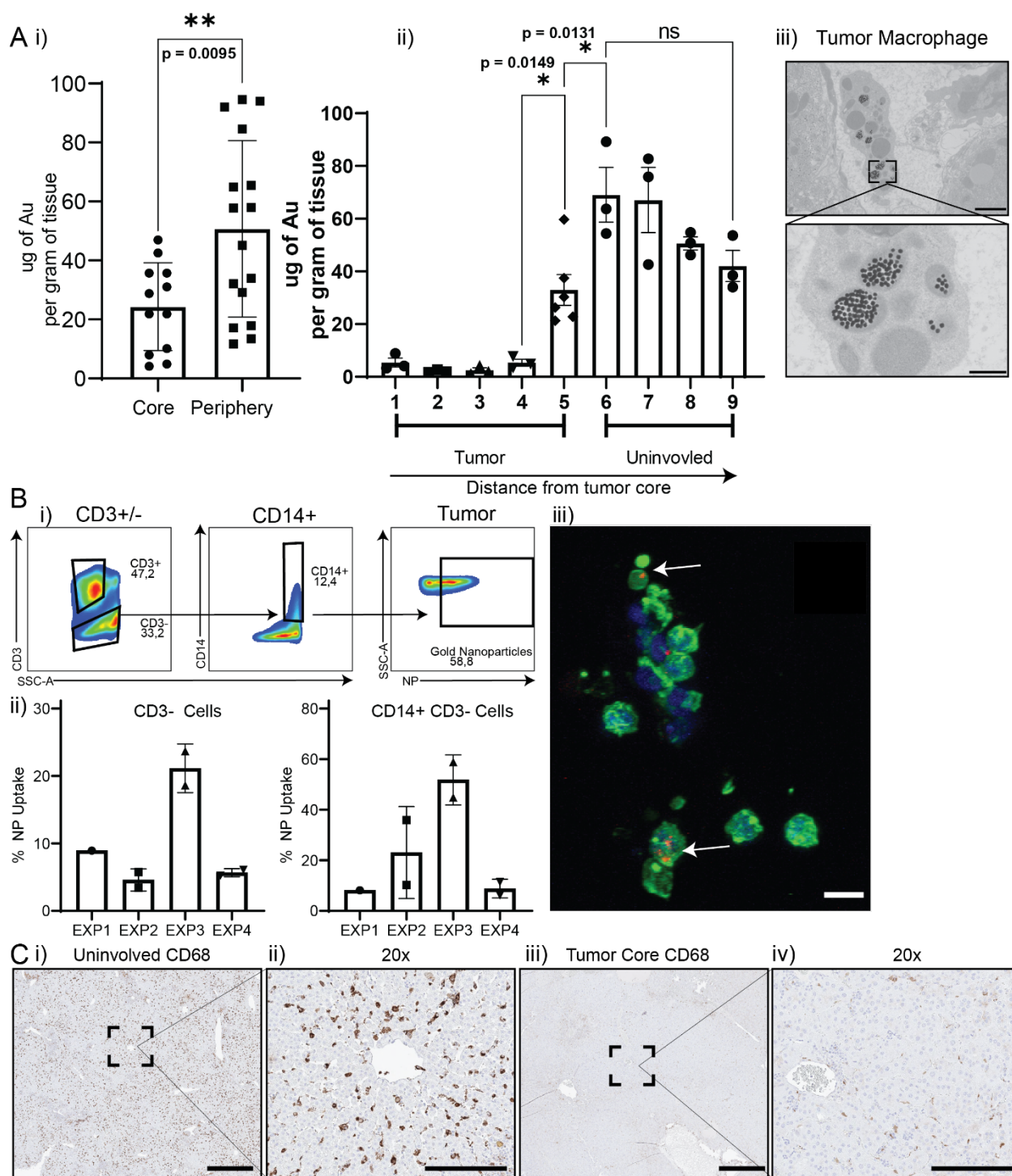


**Figure 5: Distribution of gold nanoparticles in different areas of the tumor and non-tumorous (uninvolved) tissue.** (A) Uptake of gold in  $\mu\text{g/g}$  of tissue assessed by ICP-MS. (i) Comparison of gold accumulation between tumor periphery and core of all tumor bearing animals. (ii) Assessment of NP abundance in different sections of the tumor. Each sample number (1-9) corresponds to a  $1\text{-cm}^3$  tissue slice taken from either the tumor or uninvolved tissue compartments (indicated below). Sample 1 is tissue taken from tumor core while sample 5 is tissue taken from the tumor capsule. Sample 6 is tissue at the interface between normal liver and tumor, while samples 7-9 were obtained from non-tumorous liver tissue surrounding the tumor.

1  
2  
3 Increasing sample number corresponds to increasing distance from tumor core (arrow below  
4 panel). (iii) Electron microscopy of tumor associated macrophage within tumor sinusoid (top)  
5 and magnified image of enclosed section (bottom). NPs are located in lysosomes. Scale bars  
6 represent 2  $\mu\text{m}$  (top) and 500 nm (bottom). (B) Percentage of CD14<sup>+</sup> cells from woodchuck HCC  
7 that took up NPs (i). (ii) Summary of NP uptake in cells pre-gated on CD3<sup>-</sup> (left) and CD3<sup>-</sup>  
8 CD14<sup>+</sup> (right) cells across four experiments. (iii) Confocal microscopy of magnetically sorted  
9 CD14<sup>+</sup> cells from woodchuck HCC where NPs (red) are shown (white arrows) with nuclear  
10 Hoechst (blue) and actin (green) staining. Scale represents 10  $\mu\text{m}$ . (C) Immunohistochemical  
11 staining with polyclonal anti-CD68 antibody of tumor uninvolved liver (i-ii) and tumor core (iii-  
12 iv). Scale bars denote 700  $\mu\text{m}$  and 200  $\mu\text{m}$  for 20x images. Error bars are representative of at  
13 least 2 replicates  $\pm$  SEM. Statistical significance was evaluated using unpaired t test where (\*)  
14  $< 0.05$  and (\*\*)  $< 0.01$ .  
15  
16  
17  
18  
19  
20  
21  
22  
23  
24  
25  
26  
27  
28  
29  
30  
31  
32  
33  
34  
35  
36  
37  
38  
39  
40  
41  
42  
43  
44  
45  
46  
47  
48  
49  
50  
51  
52  
53  
54  
55  
56  
57  
58  
59  
60

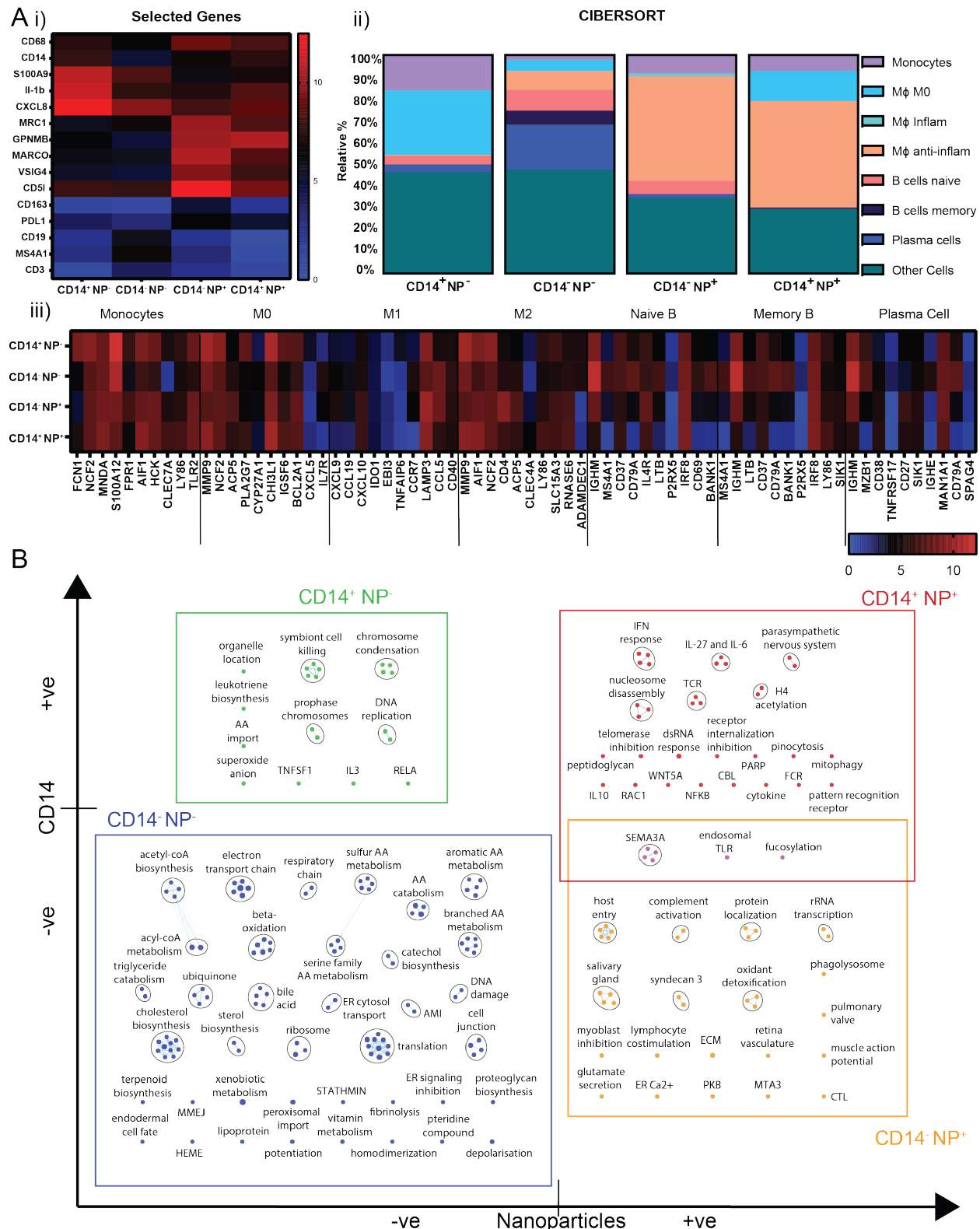


**Figure 6: RNA-seq analysis of NP+ and NP- macrophages.** (A) Gene expression profiles of FACS sorted populations from NP-treated woodchucks. (i) Selected lineage and phenotype specific genes plotted as a heat map using log<sub>2</sub>-fold expression for each of the four FACS sorted cell populations. (ii) CIBERSORT analysis of the relative proportion of immune cells from

1  
2  
3 FACS sorted cell populations of a WHV-infected liver based on RNA-sequencing. The proposed  
4 identity of the major immune cell population in each sort is shown in the associated legend for  
5 each of the four graphs. Four myeloid subpopulations (*i.e.*, Monocytes, M $\phi$  M0, M $\phi$  M  
6 inflammatory, and M $\phi$  anti-inflammatory) and three B cell subpopulations (*i.e.*, Naïve B,  
7 Memory B, and Plasma Cell) are indicated specifically, while all other immune cells were  
8 grouped into the “other” category. (iii) Corresponding expression of the top 10 genes that define  
9 an immune cell subset from CIBERSORT gene expression matrix LM22. If the gene from LM22  
10 was not identified in woodchuck, the next detected gene was plotted. Data were plotted using  
11 log<sub>2</sub>-fold expression for each of the four FACS sorted populations. (B) Gene set variation  
12 analysis (GSVA) of the four FACS sorted populations. Populations are color coded and  
13 significantly different pathways between populations are shown. A given pathway is identified  
14 by the title (black text) and each node (black circle) encompasses one or more gene sets (colored  
15 dots) that correspond to a given pathway.  
16  
17  
18  
19  
20  
21  
22  
23  
24  
25  
26  
27  
28  
29  
30  
31  
32  
33  
34  
35  
36  
37  
38  
39  
40  
41  
42  
43  
44  
45  
46  
47  
48  
49  
50  
51  
52  
53  
54  
55  
56  
57  
58  
59  
60

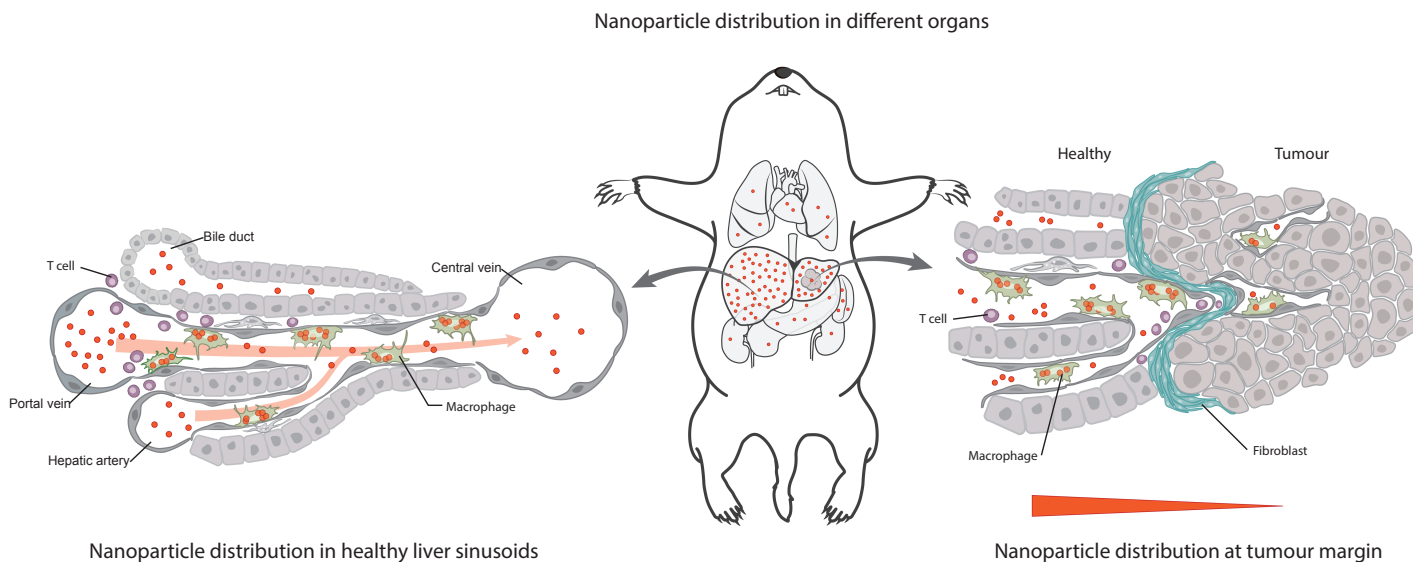
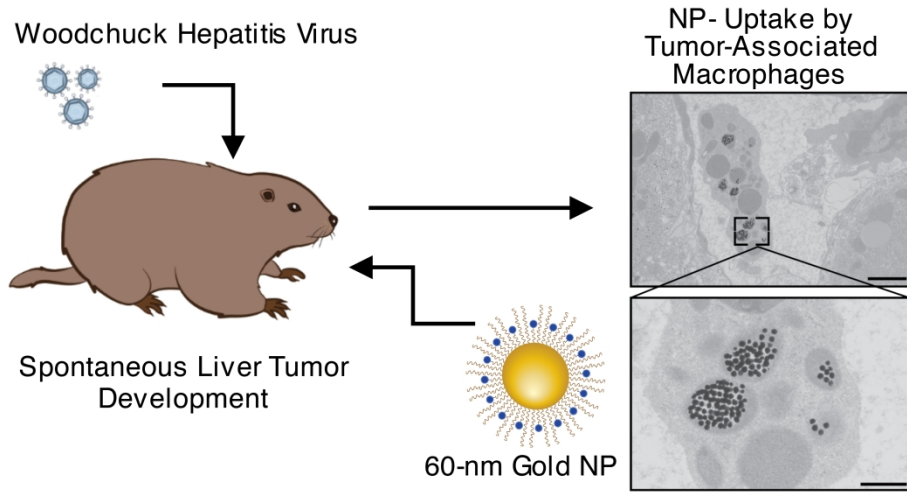


**Figure 7: Summary diagram of 60-nm gold nanoparticle uptake:** Distribution of intravenously injected 60-nm gold NPs (red dots) in different organs (middle), in sinusoid of tumor uninvolved (healthy) liver (left), and at the tumor margin (right). Density of NPs approximately correlate with findings from ICP-MS and flow cytometry experiments which indicated that the liver and spleen are the primary organs that sequester NPs. Macrophages (green cells) and T cells (purple) are shown patrolling the liver sinusoid in healthy liver tissue (left) and HCC (right). Consistent with our previous findings, macrophages within the sinusoid are depicted to sequester NPs (presence of red dots), while T cells do not accumulate NPs (absence of red dots). The tumor interface (right) depicts the area between non-tumorous and tumorous tissues shown by the segregation of essentially regular vs. dysmorphic morphology. NP abundance decreases within HCC towards the tumor core as indicated by the red gradient bar under the panel. Less macrophages were found in the tumor while the distribution of  $CD3^+$  T cells was found to be concentrated at the interface. Importantly, based on our findings from electron microscopy of tumor uninvolved and tumor tissues, hepatocytes themselves did not appear to take up 60-nm gold NPs. In general, we propose that intravenously injected gold NPs are sequestered by  $CD14^+$  cells within the liver, while resident macrophages of other organs, such as in lungs, take up NPs to a much lesser extent. Importantly, the cellular distribution of NPs seems to be specific for  $CD14^+$  cells and not for hepatocytes or T cells which supports the usage of NP-based therapies for macrophage specific targeting. Illustrations presented in this figure were designed by Joy Qu.



TOC Graphic

88x45mm (1200 x 1200 DPI)